JHEP

Published for SISSA by Springer

Received: May 1, 2015
Accepted: August 5, 2015
Published: August 24, 2015

Enhancement of the $H^{\pm}W^{\mp}Z$ vertex in the three scalar doublet model

Stefano Moretti,[a] **Diana Rojas**[a,b] **Kei Yagyu**[a]

[a] *School of Physics and Astronomy, University of Southampton, Southampton, SO17 1BJ, United Kingdom*

[b] *Instituto de Física, Benemérita Universidad Autónoma de Puebla, Apdo. Postal J-48, C.P. 72570 Puebla, Puebla, México*

E-mail: S.Moretti@soton.ac.uk, D.Rojas@soton.ac.uk, K.Yagyu@soton.ac.uk

Abstract: We compute one-loop induced trilinear vertices with physical charged Higgs bosons $H^{\pm}$ and ordinary gauge bosons, i.e., $H^{\pm}W^{\mp}Z$ and $H^{\pm}W^{\mp}\gamma$, in the model with two active plus one inert scalar doublet fields under a Z_2(unbroken) $\times$ $\tilde{Z}_2$(softly-broken) symmetry. The Z_2 and $\tilde{Z}_2$ symmetries are introduced to guarantee the stability of a dark matter candidate and to forbid the flavour changing neutral current at the tree level, respectively. The dominant form factor F_Z of the $H^{\pm}W^{\mp}Z$ vertex can be enhanced by effects of extra scalar boson loop contributions. We find that, in such a model, $|F_Z|^2$ can be one order of magnitude larger than that predicted in two Higgs doublet models, under the constraints from vacuum stability, perturbative unitarity and the electroweak precision observables. In addition, the branching fraction of the $H^{\pm} \to W^{\pm}Z$ ($H^{\pm} \to W^{\pm}\gamma$) mode can be of order 10 (1)% level when the mass of $H^{\pm}$ is below the top quark mass. Such a light $H^{\pm}$ is allowed by the so-called Type-I and Type-X Yukawa interactions which appear under the classification of the $\tilde{Z}$ charge assignment of the quarks and leptons. We also calculate the cross sections for the processes $H^{\pm} \to W^{\pm}Z$ and $H^{\pm} \to W^{\pm}\gamma$ onset by the top quark decay $t \to H^{\pm}b$ and electroweak $H^{\pm}$ production at the LHC.

Keywords: Higgs Physics, Beyond Standard Model

ArXiv ePrint: 1504.06432

doi:10.1007/JHEP08(2015)116

JHEP08(2015)116

Contents

1 Introduction **1**

2 The model **3**
- 2.1 The scalar potential 4
- 2.2 The Yukawa Lagrangian 5

3 The $H^{\pm}W^{\mp}V$ vertex **6**

4 Constraints **10**
- 4.1 Vacuum stability 10
- 4.2 Unitarity 10
- 4.3 S, T and U parameters 11
- 4.4 Flavour constraints 11
- 4.5 Direct search at LEP II 12
- 4.6 Direct search at LHC Run-I 12
- 4.7 Summary of the constraints on $m_{H^{\pm}}$ 14

5 Numerical results **14**
- 5.1 Form factors 15
- 5.2 Branching fractions of $H^{\pm}$ 17
- 5.3 Cross sections at the LHC 20

6 Conclusion **21**

A 1PI contributions **23**

JHEP08(2015)116

1 Introduction

Although the discovery of the Standard Model (SM) like Higgs boson at the Large Hadron Collider (LHC) [1–4] suggests that there is an isospin doublet scalar field in the Higgs sector, the possibility of that more Higgs doublets exist. In fact, a second doublet is often introduced in new physics models such as the Minimal Supersymmetric SM (MSSM) [5]. In addition, models with a multi-doublet structure have also been discussed based upon various physics motivations, e.g., to explain tiny neutrino masses via radiative generation [6], to provide a dark matter (DM) candidate [7] and to supply extra CP violating phases [8, 9] for the explanation of the baryon asymmetry of Universe. Thus, testing the existence of additional doublet fields is quite important to probe new physics scenarios beyond the SM.

One of the most important features of models with multi-Higgs doublets is the appearance of physical extra scalar bosons such as charged Higgs bosons $H^{\pm}$. In particular, the

properties of $H^\pm$ states strongly depend on the structure of the Higgs sector, e.g., the symmetries of the model, the actual number of doublets, the mass spectrum, etc. Therefore, through the detection of $H^\pm$ and by measuring those properties, e.g., the mass, couplings, production cross sections and decay rates, one can directly probe the existence of additional doublets as well attempt extracting the structure of the Higgs sector.

Among the various observables related to $H^\pm$, studying the $H^\pm W^\mp Z$ vertex is quite interesting because of the following features. Firstly, it has been known that the $H^\pm W^\mp Z$ vertex does not appear at the tree level[1] in multi-doublet models [10], because of an approximate global SU(2) symmetry known as the custodial symmetry[2] in the kinetic terms for the doublet fields. Secondly, although the $H^\pm W^\mp Z$ vertex is loop induced, its magnitude can be enhanced by effects of particles running in the loop, especially for the case where they come from the sector which breaks the custodial symmetry. For example, the top and bottom quark loop contributions to the $H^\pm W^\mp Z$ vertex give the quadratic dependence upon the top quark mass [11], which is responsible for the violation of the custodial symmetry in the Yukawa sector. In refs. [12, 13], the impact of extra Higgs boson loop contributions on the $H^\pm W^\mp Z$ vertex has been evaluated in the 2-Higgs Doublet Model (2HDM) [5]. It has been shown that a large mass splitting between the CP-odd Higgs boson and the charged one gives a sizable correction to the $H^\pm W^\mp Z$ vertex. From the above reasons, it is clear that the strength of the $H^\pm W^\mp Z$ vertex measures the effects of the violation of the custodial symmetry in the model embedding it. Therefore, by measuring this vertex, we can indirectly observe such a new physics effect.

Feasibility studies to measure the $H^\pm W^\mp Z$ vertex have been performed in ref. [14–16] for the LHC and in ref. [17] for future linear colliders.

In this paper, we calculate the magnitude of the $H^\pm W^\mp V$ ($V = Z, \gamma$) vertices at the one-loop level in the 3-Higgs Doublet Model (3HDM), in which the Higgs sector is composed of two *active* (with a non-zero Vacuum Expectation Value (VEV)) and one *inert* (without a non-zero VEV) doublet scalar fields. This corresponds to the simplest version of the multi-doublet model in which there is a DM candidate and an explicit CP-violating coupling in the Higgs sector. In this model, the scalar bosons from the inert doublet field give an additional contribution to the $H^\pm W^\mp V$ vertex with respect to the top/bottom quarks and scalar bosons from the active doublet loop contributions. As a phenomenological application, we also discuss how such new contributions change the decay branching fractions of the $H^\pm \to W^\pm Z$ and $H^\pm \to W^\pm \gamma$ modes and, consequently, the production cross sections involving these decay processes at the LHC.

This paper is organized as follows. In section 2, we define the Lagrangian of the 3HDM, i.e., the scalar potential and the Yukawa interactions. In section 3, we introduce the form factors of the $H^\pm W^\mp V$ vertices and discuss relationships between these form factors and effective operators. We then explain how to calculate these form factors at the one-loop level. In section 4, we summarise various constraints on the parameters of our model. From the theoretical point of view, we consider vacuum stability and perturbative unitarity. As

[1] The $H^\pm W^\mp \gamma$ vertex does also not appear at the tree level in any models with the $\mathrm{U}(1)_{\mathrm{em}}$ symmetry.

[2] In fact, the custodial symmetry is broken by the $\mathrm{U}(1)_Y$ coupling in the kinetic sector which generates the mass difference between the W and Z bosons.

JHEP08(2015)116

	$(Z_2,\ \tilde{Z}_2)$ charge								Mixing factor		
	Φ_1	Φ_2	η	Q_L	L_L	u_R	d_R	e_R	ξ_u	ξ_d	ξ_e
Type-I	$(+,+)$	$(+,-)$	$(-,+)$	$(+,+)$	$(+,+)$	$(+,-)$	$(+,-)$	$(+,-)$	$\cot\beta$	$\cot\beta$	$\cot\beta$
Type-II	$(+,+)$	$(+,-)$	$(-,+)$	$(+,+)$	$(+,+)$	$(+,-)$	$(+,+)$	$(+,+)$	$\cot\beta$	$-\tan\beta$	$-\tan\beta$
Type-X	$(+,+)$	$(+,-)$	$(-,+)$	$(+,+)$	$(+,+)$	$(+,-)$	$(+,-)$	$(+,+)$	$\cot\beta$	$\cot\beta$	$-\tan\beta$
Type-Y	$(+,+)$	$(+,-)$	$(-,+)$	$(+,+)$	$(+,+)$	$(+,-)$	$(+,+)$	$(+,-)$	$\cot\beta$	$-\tan\beta$	$\cot\beta$

Table 1. Charge assignments of the unbroken Z_2 symmetry and the softly-broken $\tilde{Z}_2$ symmetry. The mixing factors in the Yukawa interaction terms in eq. (2.14) are also shown.

experimental constraints, we take into account the bounds from the Electro-Weak (EW) S, T and U parameters, the flavour experiments and direct searches for $H^\pm$ states from LEP-II and the LHC Run-I. In section 5, we show numerical results for the form factors of the $H^\pm W^\pm V$ vertices, branching fractions of $H^\pm$ and their signal cross sections at the LHC. Our conclusion is given in section 6. In appendix, we present the full analytic expressions for the form factors of the $H^\pm W^\mp V$ vertices.

2 The model

We give a brief review of the 3HDM[3] of which the Higgs sector is composed of two active and one inert isospin doublet scalar fields [18, 19] with the hypercharge[4] $Y = +1/2$. We represent the active doublets as Φ_1 and Φ_2 whereas the inert doublet as η. Such an inert nature can be realised by assuming an unbroken Z_2 symmetry in the scalar potential, in which only η has an odd parity while all the other fields are assigned to be even. One of the important consequences of imposing such a Z_2 symmetry is that the lightest neutral scalar component in η can be a DM candidate, because it cannot decay into SM particles.

In addition to the Z_2 symmetry, we impose another Z_2 symmetry, denoted by $\tilde{Z}_2$ to distinguish it from the above one, which is required to forbid the Flavour Changing Neutral Current (FCNCs) at the tree level. This prescription is the same as that in the 2HDM [22]. For the $\tilde{Z}_2$ symmetry, we consider the softly-broken case, since avoidance of tree level FCNCs can already be achieved in this case. Under the $\tilde{Z}_2$ symmetry, four independent types of Yukawa interactions (Type-I, -II, -X and -Y) [23–26] are allowed depending on the assignment of the $\tilde{Z}_2$ charge to the SM fermions. In table 1, we show the charge assignments required by the Z_2 and $\tilde{Z}_2$ symmetries for the three scalar doublets Φ_1, Φ_2 and η and all the SM fermions, where L_L (e_R) is the left (right)-handed lepton doublet (singlet) and Q_L (u_R, d_R) is the left (right)-handed quark doublet (up-type and down-type quark singlets).

[3]The model with two inert plus one active doublets have been discussed in refs. [20, 21].

[4]We use the notation that the electric charge Q is given by $Q = T_3 + Y$ with T_3 being the third component of the isospin.

JHEP08(2015)116

2.1 The scalar potential

The most general scalar potential under the $\mathrm{SU}(2)_L \times \mathrm{U}(1)_Y \times Z_2 \times \tilde{Z}_2$ symmetry is given by

$$\begin{aligned} V(\Phi_1, \Phi_2, \eta) &= \mu_\eta^2 \eta^\dagger \eta + \mu_1^2 \Phi_1^\dagger \Phi_1 + \mu_2^2 \Phi_2^\dagger \Phi_2 - (\mu_3^2 \Phi_1^\dagger \Phi_2 + \text{h.c.}) \\ &+ \frac{1}{2}\lambda_1 (\Phi_1^\dagger \Phi_1)^2 + \frac{1}{2}\lambda_2 (\Phi_2^\dagger \Phi_2)^2 + \lambda_3 (\Phi_1^\dagger \Phi_1)(\Phi_2^\dagger \Phi_2) + \lambda_4 |\Phi_1^\dagger \Phi_2|^2 + \frac{1}{2}[\lambda_5 (\Phi_1^\dagger \Phi_2)^2 + \text{h.c.}] \\ &+ \frac{1}{2}\lambda_\eta (\eta^\dagger \eta)^2 + \rho_1 (\Phi_1^\dagger \Phi_1)(\eta^\dagger \eta) + \rho_2 |\Phi_1^\dagger \eta|^2 + \frac{1}{2}[\rho_3 (\Phi_1^\dagger \eta)^2 + \text{h.c.}] \\ &+ \sigma_1 (\Phi_2^\dagger \Phi_2)(\eta^\dagger \eta) + \sigma_2 |\Phi_2^\dagger \eta|^2 + \frac{1}{2}[\sigma_3 (\Phi_2^\dagger \eta)^2 + \text{h.c.}], \end{aligned} \tag{2.1}$$

where μ_3^2, λ_5, ρ_3 and σ_3 are complex parameters in general. Throughout the paper, we take these parameters to be real for simplicity. The scalar fields can be parameterised as

$$\Phi_i = \begin{bmatrix} w_i^+ \\ \frac{1}{\sqrt{2}}(h_i + v_i + i z_i) \end{bmatrix}, \quad (i = 1, 2), \quad \eta = \begin{bmatrix} \eta^+ \\ \frac{1}{\sqrt{2}}(\eta_H + i \eta_A) \end{bmatrix}, \tag{2.2}$$

where v_i are the VEVs of Φ_i with $v_1^2 + v_2^2 = v^2 \simeq (246\,\text{GeV})^2$. The ratio of the two VEVs is parameterized as the usual way by $\tan\beta = v_2/v_1$.

The mass formulae for the active sector are exactly the same as those in the 2HDM at the tree level. The mass eigenstates for the active scalar bosons are given as:

$$\begin{aligned} &\begin{pmatrix} w_1^\pm \\ w_2^\pm \end{pmatrix} = R(\beta) \begin{pmatrix} G^\pm \\ H^\pm \end{pmatrix}, \quad \begin{pmatrix} z_1 \\ z_2 \end{pmatrix} = R(\beta) \begin{pmatrix} G^0 \\ A \end{pmatrix}, \begin{pmatrix} h_1 \\ h_2 \end{pmatrix} = R(\alpha) \begin{pmatrix} H \\ h \end{pmatrix}, \\ &R(\theta) = \begin{pmatrix} \cos\theta & -\sin\theta \\ \sin\theta & \cos\theta \end{pmatrix}, \end{aligned} \tag{2.3}$$

where $G^\pm$ and G^0 are the Nambu-Goldstone (NG) bosons which are absorbed as their longitudinal components by the $W^\pm$ and Z bosons, respectively. We define the h state to be the SM-like Higgs boson with a mass of about 125 GeV discovered at the LHC.

The squared masses of the $H^\pm$ and A states are then calculated as

$$m_{H^\pm}^2 = M^2 - \frac{v^2}{2}(\lambda_4 + \lambda_5), \quad m_A^2 = M^2 - v^2 \lambda_5, \tag{2.4}$$

where M^2 describes the soft breaking scale of the $\tilde{Z}_2$ symmetry defined as follows

$$M^2 = \frac{\mu_3^2}{\sin\beta \cos\beta}. \tag{2.5}$$

The squared masses for the CP-even scalar states and the mixing angle α are expressed by

$$m_H^2 = \cos^2(\alpha - \beta) M_{11}^2 + \sin^2(\alpha - \beta) M_{22}^2 + \sin 2(\alpha - \beta) M_{12}^2, \tag{2.6}$$

$$m_h^2 = \sin^2(\alpha - \beta) M_{11}^2 + \cos^2(\alpha - \beta) M_{22}^2 - \sin 2(\alpha - \beta) M_{12}^2, \tag{2.7}$$

$$\tan 2(\alpha - \beta) = \frac{2 M_{12}^2}{M_{11}^2 - M_{22}^2}, \tag{2.8}$$

JHEP08(2015)116

where M^2_{ij} $(i,j = 1,2)$ are the mass matrix elements in the basis of (h'_1, h'_2) defined in eq. (3.6):

$$
\begin{aligned}
M^2_{11} &= v^2(\lambda_1 \cos^4\beta + \lambda_2 \sin^4\beta) + \frac{v^2}{2}(\lambda_3+\lambda_4+\lambda_5)\sin^2 2\beta, \\
M^2_{22} &= M^2 + v^2 \sin^2\beta \cos^2\beta \left[\lambda_1 + \lambda_2 - 2(\lambda_3+\lambda_4+\lambda_5)\right], \\
M^2_{12} &= \frac{v^2}{2}\sin 2\beta(-\lambda_1 \cos^2\beta + \lambda_2 \sin^2\beta) + \frac{v^2}{2}\sin 2\beta \cos 2\beta(\lambda_3+\lambda_4+\lambda_5).
\end{aligned} \tag{2.9}
$$

Because of the unbroken Z_2 symmetry, the scalar bosons from η do not mix with those from Φ_1 and Φ_2. Thus, the mass formulae of the inert scalar bosons are simply given by

$$
m^2_{\eta^\pm} = \mu^2_\eta + \frac{v^2}{2}\left[\rho_1 \cos^2\beta + \sigma_1 \sin^2\beta\right], \tag{2.10}
$$

$$
m^2_{\eta_H} = \mu^2_\eta + \frac{v^2}{2}\left[(\rho_1+\rho_2+\rho_3)\cos^2\beta + (\sigma_1+\sigma_2+\sigma_3)\sin^2\beta\right], \tag{2.11}
$$

$$
m^2_{\eta_A} = \mu^2_\eta + \frac{v^2}{2}\left[(\rho_1+\rho_2-\rho_3)\cos^2\beta + (\sigma_1+\sigma_2-\sigma_3)\sin^2\beta\right]. \tag{2.12}
$$

2.2 The Yukawa Lagrangian

The most general form that is invariant under the $\tilde{Z}_2$ symmetry is given by

$$
-\mathcal{L}_Y = Y_u \overline{Q}_L i\sigma_2 \Phi^*_u u_R + Y_d \overline{Q}_L \Phi_d d_R + Y_e \overline{L}_L \Phi_e e_R + \text{h.c.}, \tag{2.13}
$$

where $\Phi_{u,d,e}$ are Φ_1 or Φ_2 depending on the $\tilde{Z}_2$ charge assignment (see table 1). The interaction terms are expressed in terms of mass eigenstates of the Higgs bosons as

$$
\begin{aligned}
-\mathcal{L}^{\text{int}}_Y = &\sum_{f=u,d,e} \frac{m_{f^i}}{v}\left(\xi^f_h \overline{f}^i f^i h + \xi^f_H \overline{f}^i f^i H - 2iT^f_3 \xi_f \overline{f}^i \gamma_5 f^i A\right) \\
&+ \frac{\sqrt{2}}{v}\Big[\overline{u^i}\left(\xi_d\, V^{ij}_{\text{CKM}}\, m_{d^j} P_R - \xi_u\, m_{u^i}\, V^{ij}_{\text{CKM}}\, P_L\right) d^j\, H^+ + m_{e^i}\xi_e \overline{\nu^i} P_R e^i H^+ + \text{h.c.}\Big],
\end{aligned} \tag{2.14}
$$

where T^f_3 is the third component of the isospin for a fermion f, V^{ij}_{CKM} is the Cabibbo-Kobayashi-Maskawa matrix element, and the superscripts i and j denote the flavour indices. In eq. (2.14), ξ^f_h and ξ^f_H are defined by

$$
\xi^f_h = \sin(\beta-\alpha) + \xi_f \cos(\beta-\alpha), \tag{2.15}
$$

$$
\xi^f_H = \cos(\beta-\alpha) - \xi_f \sin(\beta-\alpha), \tag{2.16}
$$

and ξ_f in each type of Yukawa interactions are listed in table 1.

It is important to mention here that there is the so-called SM-like limit or alignment limit defined by $\sin(\beta-\alpha) \to 1$ [27, 28]. In this limit, all the h coupling constants to the SM particles acquire the same values as in the SM. In fact, the ratios of $hf\bar{f}$ and hVV couplings in our model to those in the SM are respectively given as ξ^f_h given in eq. (2.15) and $\sin(\beta-\alpha)$.

JHEP08(2015)116

3 The $H^\pm W^\mp V$ vertex

The amplitude of $H^\pm \to W^\pm V$ (relevant diagrams are shown in figure 8 in appendix A) is expressed as

$$i\mathcal{M}(H^\pm \to W^\pm V) = igm_W V_V^{\mu\nu} \epsilon_{W\mu}(p_W)\epsilon_{V\nu}(p_V), \quad \text{for} \quad V = Z,\ \gamma, \tag{3.1}$$

where $V_V^{\mu\nu}$ is written in terms of the following three dimensionless form factors:

$$V_V^{\mu\nu} = g^{\mu\nu} F_V + \frac{p_V^\mu p_W^\nu}{m_W^2} G_V + i\epsilon^{\mu\nu\rho\sigma} \frac{p_{V\rho} p_{W\sigma}}{m_W^2} H_V, \tag{3.2}$$

with p_W^μ and p_V^μ being the incoming momenta for $W^\pm$ and V, respectively. For the case of $V = \gamma$, the Ward identity guarantees the following relation;

$$V_\gamma^{\mu\nu} p_{\gamma\nu} = 0. \tag{3.3}$$

From this relation, the form factor F_γ is written as

$$F_\gamma = \frac{G_\gamma}{2}\left(1 - \frac{m_{H^\pm}^2}{m_W^2}\right), \tag{3.4}$$

where we use $p_W^2 = m_W^2$ and $(p_W + p_\gamma)^2 = m_{H^\pm}^2$.

In our model, the $H^\pm W^\mp V$ vertices do not appear at the tree level, just like in the 2HDM. This is clearly seen by introducing the so-called Higgs basis of the active scalar doublets defined as

$$\begin{pmatrix} \Phi_1 \\ \Phi_2 \end{pmatrix} = R(\beta) \begin{pmatrix} \Phi \\ \Psi \end{pmatrix}, \tag{3.5}$$

where

$$\Phi = \begin{bmatrix} G^+ \\ \frac{1}{\sqrt{2}}(h_1' + v + iG^0) \end{bmatrix}, \quad \Psi = \begin{bmatrix} H^+ \\ \frac{1}{\sqrt{2}}(h_2' + iA) \end{bmatrix}, \tag{3.6}$$

with $h_1' = H\cos(\beta-\alpha) + h\sin(\beta-\alpha)$ and $h_2' = -H\sin(\beta-\alpha) + h\cos(\beta-\alpha)$. The kinetic Lagrangian for Φ_1 and Φ_2 is then rewritten as

$$\mathcal{L}_{\rm kin} = |D_\mu \Phi_1|^2 + |D_\mu \Phi_2|^2 = |D_\mu \Phi|^2 + |D_\mu \Psi|^2, \tag{3.7}$$

where D_μ is the covariant derivative. Since the gauge-gauge-scalar type vertex is proportional to the Higgs VEV v, these vertices come from the $|D_\mu\Phi|^2$ term as only Φ has a non-zero VEV. However, the physical charged Higgs bosons $H^\pm$ are contained in the $|D_\mu\Psi|^2$ term. Therefore, the $H^\pm W^\mp Z$ vertex is absent at the tree level.[5] The above statement

[5] If we consider models which contain scalar fields with isospin larger than 1/2 such as triplets, the $H^\pm W^\mp Z$ vertex can appear at tree level. The expression for the $H^\pm W^\mp Z$ vertex can be found in refs. [10, 17] in the general extended Higgs sector which contains Higgs multiplets with the isospin T and the hypercharge Y. In addition, it has been known that in models with an extension of the gauge sector such as SU(2) × SU(2) × U(1) [29], the $H^\pm W^\mp Z$ vertex also appears at the tree level.

JHEP08(2015)116

can be generalised to a model with N active doublet scalar fields. In that case, we can also define a base transformation similar to the one of eq. (3.5). Regarding the $H^{\pm}W^{\mp}\gamma$ vertex, it does not appear at tree level in any models based on the $\mathrm{SU}(2)_L \times \mathrm{U}(1)_Y \to \mathrm{U}(1)_{\mathrm{em}}$ gauge theory, because of the $\mathrm{U}(1)_{\mathrm{em}}$ invariance and the consequent Ward identity.

The form factors defined in eq. (3.2) are introduced from the following effective Lagrangian [11, 12]:

$$\mathcal{L}_{\mathrm{eff}} = f_Z H^+ W^-_\mu Z^\mu + g_V H^+ F_W^{\mu\nu} F_{V\mu\nu} + i h_V \epsilon_{\mu\nu\rho\sigma} H^+ F_W^{\mu\nu} F_V^{\rho\sigma} + \mathrm{h.c.}, \tag{3.8}$$

where $F_W^{\mu\nu}$ and $F_V^{\mu\nu}$ are the field strength tensors for $W^{\pm}$ and V, respectively. It can be seen that the coefficient f_Z has mass dimension one whereas $g_{H^{\pm}WV}$ and h_Z have mass dimension minus one. Hence, the coefficient f_Z can be proportional to a squared mass (M_i^2) of a particle running in the loop according to a dimensional analysis:

$$f_Z \sim g g_Z \frac{M_i^2}{v} \mathcal{F}(M_i^2), \tag{3.9}$$

where $\mathcal{F}$ is a dimensionless function. Typically, it is expressed by the logarithmic function of M_i^2. On the other hand, g_Z and h_Z can be expressed as

$$g_Z,\ h_Z \sim \frac{g g_Z}{v} \mathcal{G}(M_i^2), \tag{3.10}$$

where $\mathcal{G}$ is another dimensionless function of M_i^2. Therefore, only the coefficient $f_{H^{\pm}WZ}$ can be enhanced significantly due to the M_i^2 dependence, so that the form factor F_Z gives the dominant contribution to the $H^{\pm}W^{\mp}Z$ vertex. In fact, it has been pointed out in ref. [11] that the top/bottom loop contribution to the form factor F_Z is proportional to m_t^2 only, as $m_t \gg m_b$. The origin of the quadratic dependence can be understood in terms of the Yukawa coupling $H^+ t\bar{b}$, which is proportional to m_t/v as in eq. (2.14), and of another m_t coming from the chirality flipped effect. Similarly, the quadratic mass dependence appears in the extra Higgs boson loop contribution as discussed in ref. [12]. This too can be understood, as the trilinear $H^{\pm}SS'$ (S and S' being extra scalar bosons) couplings can be rewritten by squared masses of extra scalar bosons.

Another important reason for the appearance of a M_i^2 dependence in F_Z is in relation to a violation of the custodial $\mathrm{SU}(2)_V$ symmetry. As it has been discussed in ref. [12], the dimension three term in eq. (3.8) comes from the following operator[6]

$$\mathrm{Tr}[\sigma_3 (D_\mu \mathbf{\Phi})^\dagger D^\mu \mathbf{\Psi}], \tag{3.11}$$

where $\mathbf{\Phi} = (\Phi^c, \Phi)$ and $\mathbf{\Psi} = (\Psi^c, \Psi)$ with $\Phi^c = i\sigma_2 \Phi^*$ and $\Psi^c = i\sigma_2 \Psi^*$ are the 2×2 representation form of the Higgs doublets. They are translated under the $\mathrm{SU}(2)_L \times \mathrm{SU}(2)_R$ symmetry by $\mathbf{\Phi} \to U_L \mathbf{\Phi} U_R^\dagger$ and $\mathbf{\Psi} \to U_L \mathbf{\Psi} U_R^\dagger$, where U_L and U_R are respectively the $\mathrm{SU}(2)_L$ and $\mathrm{SU}(2)_R$ unitary transformation matrices. We can see that the operator given in eq. (3.11) is not invariant under the $\mathrm{SU}(2)_R$ transformation, so that this operator

[6]The operator $\mathrm{Tr}[D_\mu \mathbf{\Phi} D^\mu \mathbf{\Psi}]$ also gives the $H^{\pm}W^{\mp}Z$ term in the effective Lagrangian which is proportional to $\sin^2\theta_W$. However, such an effect is cancelled by the counter term of the $H^{\pm}WZ$ vertex.

JHEP08(2015)116

breaks the $SU(2)_R$ invariance. Since the custodial $SU(2)_V$ symmetry corresponds to the remaining symmetry after the EW symmetry breaking, i.e., $SU(2)_L \times SU(2)_R \to SU(2)_V$ and a violation of the $SU(2)_R$ symmetry means a violation of the $SU(2)_V$ symmetry.

Therefore, the quadratic mass dependence in F_Z can be understood as a result of the custodial symmetry breaking. In fact, it has been known that the mass difference between the top and bottom quarks gives the violation of the custodial symmetry in the Yukawa sector. In addition, that between A and $H^\pm$ also gives the violation of the custodial symmetry in the Higgs potential [30]. Since the top quark mass is already known by experiments, the top quark loop contribution to the $H^\pm W^\mp Z$ vertex is determined by its mass.[7] In contrast, parameters in the scalar sector have not yet determined by experiments except for the Higgs boson mass of about 125 GeV, so that we can expect a sizable enhancement of the $H^\pm W^\mp Z$ vertex from scalar boson loop effects in suitable regions of the 3HDM parameter space.

In the following, we discuss how we calculate the form factors of the $H^\pm W^\mp V$ vertices. We can separately consider the one-loop contributions to the vertices from the 1PI diagrams and the counter terms as

$$(F_V, G_V, H_V) = (F_V^{\rm 1PI} + \delta F_V,\ G_V^{\rm 1PI} + \delta G_V,\ H_V^{\rm 1PI} + \delta H_V), \tag{3.12}$$

where $X_V^{\rm 1PI}$ and δX_V are respectively the 1PI and the counter term contributions to the form factor X_V ($X = F,\ G$ and H). Their analytic expressions are given in appendix A.

The counter term contributions are obtained as follows. First, we define the renormalized two point function for the $W^\pm$-$H^\pm$ mixing as

$$\hat{\Gamma}^\mu_{WH}(p^2) = (-ip^\mu)\hat{\Gamma}_{WH}(p^2), \tag{3.13}$$

where p^μ is the incoming four momentum of $H^\pm$. The renormalised form factor $\hat{\Gamma}_{WH}$ is given by

$$\hat{\Gamma}_{WH}(p^2) = im_W\delta_{GH} + \Gamma^{\rm 1PI}_{WH}(p^2), \tag{3.14}$$

where δ_{GH} is the counter term for the $G^\pm$-$H^\pm$ mixing, and $\Gamma^{\rm 1PI}_{WH}$ is the 1PI diagram contribution to the $W^\pm$-$H^\pm$ mixing as shown in figure 9. The analytic expression of $\Gamma^{\rm 1PI}_{WH}$ is given in appendix A. The counter term is obtained by the shift of the charged NG boson field $G^\pm$:

$$G^\pm \to (1 + \delta Z_G/2)G^\pm + \delta_{GH}H^\pm. \tag{3.15}$$

By imposing the on-shell renormalisation condition [31, 32]

$$\hat{\Gamma}_{WH}(p^2 = m^2_{H^\pm}) = 0, \tag{3.16}$$

we can determine the counter term

$$\delta_{GH} = i\frac{\Gamma^{\rm 1PI}_{WH}(p^2 = m^2_{H^\pm})}{m_W}. \tag{3.17}$$

[7] In our model, the top quark loop contribution also depends on $\tan\beta$, and in all the four types of Yukawa interactions, its dependence is given by $\cot\beta$.

JHEP08(2015)116

We then obtain the counter term contribution to the $H^\pm W^\mp V$ vertex as

$$\begin{aligned}\mathcal{L}_{GWV} &= -\frac{g}{c_W} m_W s_W^2 G^+ W_\mu^- Z^\mu + e m_W G^+ W^- A_\mu + \text{h.c.} \\ &\to -\frac{g}{c_W} m_W s_W^2 \delta_{GW} H^+ W_\mu^- Z^\mu + e m_W \delta_{GW} H^+ W_\mu^- A^\mu + \cdots,\end{aligned} \tag{3.18}$$

where $s_W = \sin\theta_W$ and $c_W = \cos\theta_W$ with θ_W being the weak mixing angle. From eqs. (3.17) and (3.18), δF_V is given by

$$\delta F_Z = -i\frac{s_W^2}{c_W}\frac{\Gamma_{WH}^{\text{1PI}}(p^2 = m_{H^\pm}^2)}{m_W}, \quad \delta F_\gamma = i s_W \frac{\Gamma_{WH}^{\text{1PI}}(p^2 = m_{H^\pm}^2)}{m_W}. \tag{3.19}$$

We then obtain the finite results for the form factors of the $H^\pm W^\mp Z$ and $H^\pm W^\mp \gamma$ vertices. In the case of $\sin(\beta-\alpha) = 1$, $m_H = m_A$, $m_A \gg m_{H^\pm}$, $m_{\eta_H} = m_{\eta_A}$ and $m_{\eta_A} \gg m_{\eta^\pm}$, we obtain

$$F_Z \simeq \frac{\cot\beta}{16\pi^2 v^2 c_W}\left[N_c m_t^2 + \frac{M^2 - m_A^2}{2}(\tan^2\beta - 1) + \left(m_{\eta_A}^2 - m_{\eta^\pm}^2 - \frac{v^2}{2}\rho_2\right)\right], \tag{3.20}$$

where the first, second and third terms correspond to the contributions from t-b, active and inert scalar boson loops, respectively. We here note that the parameter M^2 defined in eq. (2.5) appearing in the second term in eq. (3.20) is not relevant to the Higgs VEV, and if $M^2 < v^2$, the masses of extra active scalar bosons are mainly given from v^2. From the above expression, we can clearly see the quadratic mass dependences m_t^2, m_A^2 and $m_{\eta_A}^2$. However, as it will be discussed in the next section, the case considered in the above, i.e., $m_H = m_A \gg m_{H^\pm}$ and $m_{\eta_H} = m_{\eta_A} \gg m_{\eta^\pm}$ also gives the similar quadratic dependence in the EW T parameter. Therefore, too large mass difference between $H^\pm$ and A (with $m_H = m_A$) and that between $\eta^\pm$ and η_A (with $m_{\eta_H} = m_{\eta_A}$) are not allowed. Instead of taking the above case, we can consider the case with $\sin(\beta-\alpha) = 1$, $m_A \gg m_{H^\pm}(= m_H)$ and $m_{\eta_A} \gg m_{\eta^\pm}(= m_{\eta_H})$, where the contribution to the T parameter from extra scalar boson loops is cancelled. We then obtain

$$F_Z \simeq \frac{\cot\beta}{16\pi^2 v^2 c_W}\left[N_c m_t^2 + (M^2 - m_{H^\pm}^2)(\tan^2\beta - 1)F\left(\frac{m_{H^\pm}^2}{m_A^2}\right) - \frac{v^2}{2}(\rho_2 + \rho_3)F\left(\frac{m_{\eta^\pm}^2}{m_{\eta_A}^2}\right)\right], \tag{3.21}$$

where $N_c = 3$ is the color factor, and the function F is given by

$$F(r) = -\frac{1}{4(1-r)^2}\left[3 - 4r + r^2 + 2(2-r)r\ln r\right] - \frac{1}{2}\ln r. \tag{3.22}$$

This function has the following asymptotic behavior:

$$F(r) \simeq -\frac{3}{4} - \frac{1}{2}\ln r \quad \text{for} \quad r \ll 1, \quad F(r) \simeq -\frac{1}{4} \quad \text{for} \quad r \gg 1, \quad F(r) \simeq \frac{1-r}{2} \quad \text{for} \quad r \simeq 1. \tag{3.23}$$

In this case, although the quadratic dependence of F_Z on m_A^2 and $m_{\eta_A}^2$ disappears, there still remains their logarithmic dependence.

JHEP08(2015)116

4 Constraints

4.1 Vacuum stability

The stability condition for the Higgs potential is given by requiring that the Higgs potential is bounded from below in any direction of the scalar boson space. The necessary and sufficient condition to guarantee such a positivity of the potential has been derived in ref. [19] as

$$\lambda_\eta > 0, \quad \lambda_1 > 0, \quad \lambda_2 > 0, \tag{4.1}$$

$$\sqrt{\lambda_1\lambda_2} + \bar{\lambda} > 0, \quad \sqrt{\lambda_\eta\lambda_1} + \bar{\rho} > 0, \quad \sqrt{\lambda_\eta\lambda_2} + \bar{\sigma} > 0, \tag{4.2}$$

$$\sqrt{\lambda_\eta}\bar{\lambda} + \sqrt{\lambda_1}\bar{\sigma} + \sqrt{\lambda_2}\bar{\rho} > 0 \ \text{ or } \ \lambda_\eta\bar{\lambda}^2 + \lambda_1\bar{\sigma}^2 + \lambda_2\bar{\rho}^2 - \lambda_\eta\lambda_1\lambda_2 - 2\bar{\lambda}\bar{\rho}\bar{\sigma} < 0, \tag{4.3}$$

$$\begin{aligned}
\bar{\lambda} &= \lambda_3 + \text{MIN}(0,\ \lambda_4 + \lambda_5,\ \lambda_4 - \lambda_5),\\
\bar{\rho} &= \rho_1 + \text{MIN}(0,\ \rho_2 + \rho_3,\ \rho_2 - \rho_3),\\
\bar{\sigma} &= \sigma_1 + \text{MIN}(0,\ \sigma_2 + \sigma_3,\ \sigma_2 - \sigma_3).
\end{aligned} \tag{4.4}$$

4.2 Unitarity

Some combinations of scalar quartic couplings are constrained from perturbative unitarity. In the 3HDM, the s wave amplitude matrix for all the 2-to-2 body scalar boson elastic scatterings have been calculated in ref. [33] in the high energy limit. We obtain the following independent eigenvalues or sub-matrices for the s wave amplitude matrix as

$$X_1 = \begin{pmatrix} 3\lambda_\eta & 2\rho_1+\rho_2 & 2\sigma_1+\sigma_2 \\ 2\rho_1+\rho_2 & 3\lambda_1 & 2\lambda_3+\lambda_4 \\ 2\sigma_1+\sigma_2 & 2\lambda_3+\lambda_4 & 3\lambda_2 \end{pmatrix}, \ X_2 = \begin{pmatrix} \lambda_\eta & \rho_2 & \sigma_2 \\ \rho_2 & \lambda_1 & \lambda_4 \\ \sigma_2 & \lambda_4 & \lambda_2 \end{pmatrix}, \ X_3 = \begin{pmatrix} \lambda_\eta & \rho_3 & \sigma_3 \\ \rho_3 & \lambda_1 & \lambda_5 \\ \sigma_3 & \lambda_5 & \lambda_2 \end{pmatrix}, \tag{4.5}$$

$$y_1^\pm = \lambda_3 + 2\lambda_4 \pm 3\lambda_5, \tag{4.6}$$

$$y_2^\pm = \rho_1 + 2\rho_2 \pm 3\rho_3, \tag{4.7}$$

$$y_3^\pm = \sigma_1 + 2\sigma_2 \pm 3\sigma_3, \tag{4.8}$$

$$y_4^\pm = \lambda_3 \pm \lambda_5, \tag{4.9}$$

$$y_5^\pm = \rho_1 \pm \rho_3, \tag{4.10}$$

$$y_6^\pm = \sigma_1 \pm \sigma_3, \tag{4.11}$$

$$y_7^\pm = \lambda_3 \pm \lambda_4, \tag{4.12}$$

$$y_8^\pm = \rho_1 \pm \rho_2, \tag{4.13}$$

$$y_9^\pm = \sigma_1 \pm \sigma_2. \tag{4.14}$$

We then require the following condition:

$$|x_i| < 8\pi, \quad |y_j^\pm| < 8\pi, \quad (i,j = 1,\ldots 9), \tag{4.15}$$

where x_i are the eigenvalues of X_1, X_2 and X_3.

JHEP08(2015)116

4.3 S, T and U parameters

The EW oblique parameters S, T and U [34] can be modified from the SM prediction by the extra scalar boson loop contributions and the modified SM-like Higgs boson couplings. The differences in the predictions of the S, T and U parameters in the 3HDM and those in the SM are given in the case with $\sin(\beta-\alpha)=1$, $m_H = m_A$, $m_{\eta_H} = m_{\eta^\pm}$ as

$$\Delta T \simeq \frac{1}{24\pi^2 \alpha_{\rm em} v^2}(m_{H^\pm} - m_A)^2, \tag{4.16}$$

$$\Delta U \simeq \frac{1}{12\pi}\Big(\ln\frac{m_A^2}{m_{H^\pm}^2} + \frac{2m_{H^\pm}}{m_A} - 2\Big) \simeq 0, \tag{4.17}$$

assuming $m_A \simeq m_{H^\pm}$, and

$$\Delta S \simeq \frac{1}{12\pi}\Big(\ln\frac{m_A^2}{m_{H^\pm}^2} + \ln\frac{m_{\eta_A}^2}{m_{\eta^\pm}^2} - \frac{5}{6}\Big), \quad \text{for} \quad m_{\eta_A} \gg m_{\eta^\pm}, \tag{4.18}$$

$$\Delta S \simeq \frac{1}{12\pi}\Big(\ln\frac{m_A^2}{m_{H^\pm}^2} - \frac{5}{6}\Big), \quad \text{for} \quad m_{\eta^\pm} \gg m_{\eta_A}, \tag{4.19}$$

$$\Delta S \simeq \frac{1}{12\pi}\Big(\ln\frac{m_A^2}{m_{H^\pm}^2} + \frac{m_{\eta_A}}{m_{\eta^\pm}} - 1\Big) \simeq 0, \quad \text{for} \quad m_{\eta^\pm} \simeq m_{\eta_A}. \tag{4.20}$$

The general expression is given in ref. [33]. From the global fit of the EW precision data, ΔS and ΔT are extracted by fixing $\Delta U = 0$ as

$$\Delta S = 0.05 \pm 0.09, \quad \Delta T = 0.08 \pm 0.07, \tag{4.21}$$

with the correlation coefficient of $+0.91$ [35].

In figure 1, we show the constraint from the S and T parameters on the m_A-m_{η_A} plane. We take $\sin(\beta-\alpha)=1$, $m_H = m_A$ and $m_{\eta^\pm} = m_{\eta_H} = m_A/2$, which is also taken in the numerical results shown in section 5. In the left and right panel, $m_{H^\pm}$ is fixed to be 150 GeV and 200 GeV, respectively. We can see that, for $m_{\eta_A} \simeq m_{\eta^\pm}$, a magnitude of the mass splitting between A and $H^\pm$ to be larger than about 75 GeV is excluded by the T parameter due to the quadratic dependence of the mass splitting shown in eq. (4.16). In this case, the contribution to ΔS is almost zero as it is seen in eq. (4.20). Conversely, in the case of $m_{\eta_A} \gg m_{\eta^\pm}$, the positive logarithmic contribution to ΔS appears as shown in eq. (4.18) and a too large mass splitting between η_A and $\eta^\pm$ is excluded by ΔS. However, the constraint from ΔS is getting milder when there is a positive contribution to ΔT, because of the positive correlation between ΔS and ΔT. Therefore, in order to have a large mass splitting between η_A and $\eta^\pm$, which is required to obtain a significant contribution to the $H^\pm W^\mp Z$ vertex, we need a mass splitting between A and $H^\pm$.

4.4 Flavour constraints

We can apply the same constraints from the B physics measurements as those in the 2HDM to our 3HDM, because of the same structure of the active sector. From the $b \to s\gamma$ process, the mass bound of $m_{H^\pm} \gtrsim 480$ GeV [36] is given at 95% confidence level (CL) in models

JHEP08(2015)116

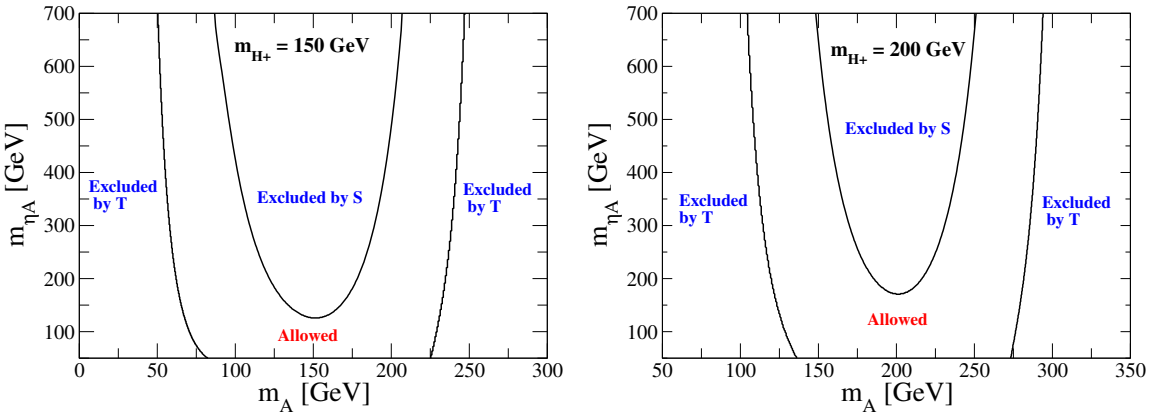

Figure 1. Constraint from the S and T parameters on the m_A-m_{η_A} plane in the case of $m_H = m_A$, $\sin(\beta - \alpha) = 1$ and $m_{\eta^\pm} = m_{\eta_H} = m_A/2$. The charged Higgs boson mass is fixed to be 150 GeV (left panel) and 200 GeV (right panel). The 95% CL excluded regions are indicated in the figure.

with the Type-II and Type-Y Yukawa interactions with $\tan\beta \gtrsim 2$ via the next-to-next-to-leading order calculation [36–38]. This bound is getting stronger when a smaller value of $\tan\beta$ is considered. In models with Type-I and Type-X Yukawa interactions, the constraint from $b \to s\gamma$ is only important in the small $\tan\beta$ case. For instance, the lower limit on $m_{H^\pm}$ is given to be about 100, 200 and 800 GeV at 95% CL in the cases of $\tan\beta = 2.5$, 2 and 1, respectively [38].

The B^0-$\bar{B}^0$ mixing also gives a bound on $m_{H^\pm}$, especially for small $\tan\beta$'s. In the case of $\tan\beta = 1$, $m_{H^\pm} \lesssim 500$ GeV is excluded at 95% CL in models with all the types of Yukawa interactions [39], which is stronger than the constraint from $b \to s\gamma$ for the Type-II and Type-Y cases. This bound becomes rapidly weaker when we consider $\tan\beta \gtrsim 1$, e.g., for $\tan\beta = 1.5$ (2), the limit is $m_{H^\pm} \lesssim 300$ (100) GeV at 95% CL.

4.5 Direct search at LEP II

At the LEP II experiment, charged Higgs bosons have been searched via the $e^+e^- \to Z^*/\gamma^* \to H^+H^-$ process [40]. From the non-observation of a significant excess, the lower mass limit has been taken to be about 80 GeV at 95% CL under the assumption of $\mathrm{BR}(H^\pm \to \tau^\pm\nu) + \mathrm{BR}(H^\pm \to cs) = 1$. The slightly stronger bound $m_{H^\pm} \gtrsim 90$ GeV can be obtained assuming $\mathrm{BR}(H^\pm \to \tau^\pm\nu) = 1$.

4.6 Direct search at LHC Run-I

At the LHC, $H^\pm$ searches have been performed for the two cases: the low mass region $m_{H^\pm} < m_t + m_b$ and the high mass region $m_{H^\pm} > m_t + m_b$. For the low mass case, the $t \to H^+b$ decay is used as the $H^\pm$ production mode and the full process $pp \to t\bar{t} \to b\bar{b}H^\pm W^\mp$ with the $H^\pm \to \tau^\pm\nu$ decay has thus been analysed. Using the data obtained at $\sqrt{s} = 8$ TeV after 19.5 fb^{-1} of the integrated luminosity, the upper limit on the product of branching ratios $\mathrm{BR}(t \to H^\pm b) \times \mathrm{BR}(H^\pm \to \tau^\pm\nu)$ has been obtained to be between 0.23% and 1.3% at 95% CL for $m_{H^\pm}$ in the range of 80 GeV to 160 GeV [41].

JHEP08(2015)116

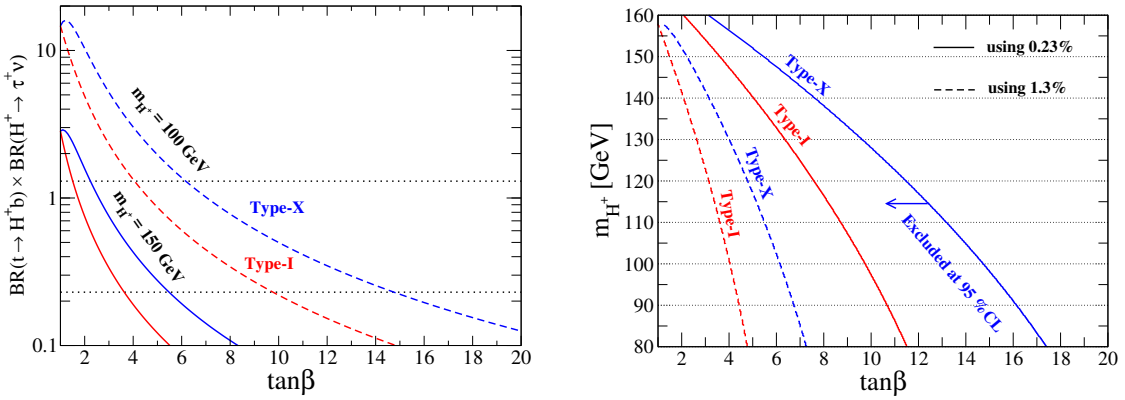

Figure 2. (Left panel) The product of branching fractions BR($t \to H^+b$)×BR($H^+ \to \tau^+\nu$) as a function of $\tan\beta$ in the Type-I (red curves) and Type-X (blue curves) 2HDMs/3HDMs. We take $m_{H^\pm} = m_A = m_H = M$ and $\sin(\beta-\alpha) = 1$ in this plot. The dashed and solid curves respectively show the cases of $m_{H^\pm}$ =100 GeV and 150 GeV. The horizontal dotted lines show the upper limits (0.23% and 1.3%) from the LHC data. (Right) Excluded parameter regions on the $\tan\beta$-$m_{H^\pm}$ plane in the Type-I and Type-X 2HDMs/3HDMs. Regions inside from each curve are excluded at 95% CL by the measurement of top decay $t \to H^\pm b \to \tau^\pm b\nu$. The solid and dashed curves are the results using the upper limit on BR($t \to H^+b$)×BR($H^+ \to \tau^+\nu$) to be 0.23% and 1.3%, respectively.

In the left panel of figure 2, the above product of branching ratios is shown as a function of $\tan\beta$ in the Type-I and Type-X 2HDMs. Because the light $H^\pm$ scenario, i.e., $m_{H^\pm} < m_t$, in the Type-II and Type-Y 2HDMs has already been excluded by $b \to s\gamma$ data as explained in section 4.4, we here only show the Type-I and Type-X cases. In the Type-X 2HDM, the product of the branching fractions is slightly larger than that in the Type-I 2HDM. This can be understood in such a way that in the Type-X 2HDM the branching fraction of $H^\pm \to \tau^\pm\nu$ is enhanced as $\tan\beta$ is increased, while it does not depend on $\tan\beta$ in the Type-I 2HDM. For example, BR($H^+ \to \tau^+\nu$) can be almost 100% when $\tan\beta \gtrsim 3$ in the Type-I 2HDM, but it is about 40% in the Type-I 2HDM. In contrast, the branching ratio of $t \to H^+b$ is given by the same value in both Type-I and Type-X 2HDMs. Therefore, a bit stronger bound on $\tan\beta$ for a fixed value of $m_{H^\pm}$ is obtained in the Type-X 2HDM. For example, if we use the stronger bound for BR($t \to H^\pm b$)×BR($H^\pm \to \tau^\pm\nu$), i.e., 0.23%, $\tan\beta \lesssim 6$ (4) and 15 (10) are excluded for $m_{H^\pm} = 100$ and 150 GeV in the Type-X (Type-I) 2HDM.

For the high $H^\pm$ mass region, i.e., $m_{H^\pm} > m_t$, the production process $gb \to tH^\pm$ (i.e., $H^\pm$-strahlung) can be used instead of the top quark decay.[8] The 95% CL upper limit on the cross section times branching ratio $\sigma(pp \to tH^\pm + X) \times$ BR($H^\pm \to \tau^\pm\nu$) has been given to be between 0.76 pb and 4.5 fb in the range of $m_{H^\pm}$ =180 GeV to 1 TeV [41]. This limit gives an upper limit on $\tan\beta$ for a fixed value of $m_{H^\pm}$ in the 2HDMs. For example, $\tan\beta \gtrsim 50$ (60) at $m_{H^\pm} = 200$ (230) GeV can be excluded at 95% CL in the MSSM [41], where a similar bound is expected to be obtained in the Type-II 2HDM because of the same

[8]Notice that we have emulated both the top quark production and the decay as well as $H^\pm$-strahlung through the single $gg \to tbH^\pm$ mode, in the spirit of [42].

JHEP08(2015)116

Experiment	95% CL lower lim. on $m_{H^\pm}$	$\tan\beta$	Type	Comments
$b \to s\gamma$	480 GeV	-	II and Y	
	(800, 200, 100) GeV	(1, 2, 2.5)	I and X	
B^0-$\bar{B}^0$	(500, 300, 100) GeV	(1, 1.5, 2)	All	
LEP II	(80, 90) GeV	-	All	$\mathcal{B}_{\tau\nu} + \mathcal{B}_{cs} = 1$, $\mathcal{B}_{\tau\nu} = 1$
$t \to H^\pm b$	(160, 140, 100) GeV	(1, 2, 4)	I	Using 1.3% (See figure 2)
at the LHC Run-I	(160, 150, 130) GeV	(1, 2, 4)	X	Using 1.3% (See figure 2)

Table 2. The 95% CL lower bound on $m_{H^\pm}$ in the 2HDMs/3HDMs from various experimental measurements for a fixed value of $\tan\beta$. For the row of LEP II, 80 (90) GeV is given for the case of $\mathcal{B}_{\tau\nu} + \mathcal{B}_{cs} = 1$, ($\mathcal{B}_{\tau\nu} = 1$), where $\mathcal{B}_{\tau\nu}$ and $\mathcal{B}_{cs}$ are the branching fractions of $H^\pm \to \tau^\pm\nu$ and $H^\pm \to cs$ modes, respectively.

structure of the Yukawa interaction.[9] In the Type-I and Type-X 2HDMs, the production cross section of $pp \to tH^\pm + X$ is significantly suppressed by a factor $\cot^2\beta$, so that we cannot expect to obtain an important bound in the high mass region.

4.7 Summary of the constraints on $m_{H^\pm}$

In table 2, we present the summary of the current experimental bounds on $m_{H^\pm}$ in the 2HDMs/3HDMs with the four types of Yukawa interactions from various experimental observations.

5 Numerical results

In this section, we perform numerical evaluations for the $H^\pm W^\mp V$ vertices and related observables. In particular, we focus on the light $H^\pm$ case, i.e, $m_{H^\pm} = \mathcal{O}(100)$ GeV, because of its phenomenological interest. As we discussed in section 4, such a scenario is allowed in the Type-I and Type-X Yukawa interactions from flavour constraints, so that we consider these types only in this section. First, we evaluate the form factors of the $H^\pm W^\mp Z$ and $H^\pm W^\mp \gamma$ vertices. For the $H^\pm W^\mp \gamma$ vertex, since the form factor F_γ is related to G_γ by the Ward identity, we only show G_γ and H_γ. Second, we show all the branching fractions of $H^\pm$, including the $H^\pm \to W^\pm Z$ and $H^\pm \to W^\pm\gamma$ modes. Finally, we discuss cross sections for various signal processes involving the $H^\pm \to W^\pm Z$ and $H^\pm \to W^\pm\gamma$ decays at the LHC.

In our model, there are 16 independent parameters in the potential given in eq. (2.1), namely, $\mu^2_{1\text{-}3}$, μ^2_η, $\lambda_{1\text{-}5}$, λ_η, $\rho_{1\text{-}3}$ and $\sigma_{1\text{-}3}$. They are divided into 8 parameters in the active sector ($\mu^2_{1\text{-}3}$ and $\lambda_{1\text{-}5}$) and the remaining 8 parameters (μ^2_η, λ_η, $\rho_{1\text{-}3}$ and $\sigma_{1\text{-}3}$).

After the tadpole conditions are imposed, the former 8 parameters can be expressed by v, $\tan\beta$, $\sin(\beta-\alpha)$ m_h, m_H, m_A, $m_{H^\pm}$ and M^2. Two of the 8 parameters, v and m_h,

[9] In the Type-Y 2HDM, although the same production cross section of $pp \to tH^\pm + X$ is obtained as in the Type-II case, the branching fraction of $H^\pm \to \tau^\pm\nu$ is significantly suppressed due to the enhancement of the decay rate of the $H^\pm \to bc$ mode [43, 44]. Therefore, the bound in the Type-Y 2HDM can be much weaker than that in the Type-II case.

JHEP08(2015)116

should be used to reproduce the gauge boson masses and the observed Higgs boson mass, i.e., $v \simeq 246\,\text{GeV}$ and $m_h \simeq 125\,\text{GeV}$. Furthermore, the Higgs boson search data at the LHC suggests that the observed Higgs boson is SM-like [1–4], so that taking $\sin(\beta-\alpha) \approx 1$ gives a good benchmark scenario as we explained in section 2. We thus take $\sin(\beta-\alpha) = 1$ in the following calculation.

Regarding the latter 8 parameters, we proceed as follows. First, we take $\lambda_\eta = 0$, as this gives a four-point interaction among the inert scalar bosons that does not affect the following analysis. Second, we take ρ_1 and σ_1 so as to satisfy the vacuum stability condition given in eqs. (4.2) and (4.3) for given values of $\rho_{2,3}$ and $\sigma_{2,3}$:

$$\rho_1 = \text{MIN}(0, \rho_2+\rho_3, \rho_2-\rho_3), \quad \sigma_1 = \text{MIN}(0, \sigma_2+\sigma_3, \sigma_2-\sigma_3). \tag{5.1}$$

Finally, the remaining 5 parameters can be expressed in terms of three masses of the inert scalar bosons ($m_{\eta^\pm}$, m_{η_A} and m_{η_H}) and the ρ_2 and ρ_3 parameters. In this parametrisation, the σ_2 and σ_3 parameters are given as the outputs:

$$\sigma_2 = -\rho_2 \cot^2\beta + \frac{1}{v^2\sin^2\beta}\left(m^2_{\eta_A} + m^2_{\eta_H} - 2m^2_{\eta^\pm}\right), \tag{5.2}$$

$$\sigma_3 = -\rho_3 \cot^2\beta + \frac{1}{v^2\sin^2\beta}\left(m^2_{\eta_H} - m^2_{\eta_A}\right). \tag{5.3}$$

Therefore, to recap, we are left with 5 new parameters in the active sector ($\tan\beta$, $m_{H^\pm}$, m_A, m_H and M^2) and 5 new ones in the inert sector too ($m_{\eta^\pm}$, m_{η_A}, m_{η_H}, ρ_2 and ρ_3) and we will scan over these. Regarding the SM inputs, we use the following values [45, 46]:

$$\begin{aligned}
&m_Z = 91.1876\ \text{GeV}, \ m_W = 80.385\ \text{GeV}, && G_F = 1.1663787\times10^{-5}\ \text{GeV}^{-2},\\
&m_t = 173.07\ \text{GeV}, \quad m_b = 3.0\ \text{GeV}, \ m_c = 0.677\ \text{GeV}, && V^{cb}_{\text{CKM}} = 0.0409,\ V^{ts}_{\text{CKM}} = 0.0429,\\
&m_\tau = 1.77684\ \text{GeV}, \ m_\mu = 0.105658367\ \text{GeV}, && m_h = 125\ \text{GeV}.
\end{aligned} \tag{5.4}$$

where the quark masses m_b and m_c are given at the m_Z scale as quoted from ref. [46].

The form factors depend on the three momenta p^μ_W, p^μ_V and $q^\mu = p^\mu_W + p^\mu_V$ for W, V $(= Z, \gamma)$ and $H^\pm$, respectively. In the numerical calculation, when $m_{H^\pm} \geq m_W + m_Z$, we take $p^2_W = m^2_W$, $p^2_Z = m^2_Z$ and $q^2 = m^2_{H^\pm}$ while when $m_{H^\pm} < m_W + m_Z$, we take $p^2_W = (m_{H^\pm} - m_Z)^2$, $p^2_Z = m^2_Z$ and $q^2 = m^2_{H^\pm}$ (thereby allowing for below threshold $H^\pm$ decays too). For the $H^\pm W^\mp\gamma$ vertex, we take $p^2_W = m^2_W$, $p^2_\gamma = 0$ and $q^2 = m^2_{H^\pm}$.

5.1 Form factors

We start by showing the numerical results of the form factors of the $H^\pm W^\mp Z$ and $H^\pm W^\mp\gamma$ vertices. In order to see how the inert scalar boson loops can change the prediction, we first show the result in the 2HDM under the constraints from unitarity, vacuum stability and the EW parameters as discussed in section 4. Then, we move on to the 3HDM.

In figure 3, the values of $|X_Z|^2$ ($X = F$, G and H) and $|Y_\gamma|^2$ ($Y = G$ and H) are respectively plotted in the upper and lower panels as a function of $\tan\beta$ in the case of $\sin(\beta-\alpha) = 1$ and $m_H = m_{H^\pm}$. The left (right) panel shows the case of $m_{H^\pm} = 150$ (200) GeV. The solid, dashed and dotted (dashed and dotted) curves respectively show the fermion loop

JHEP08(2015)116

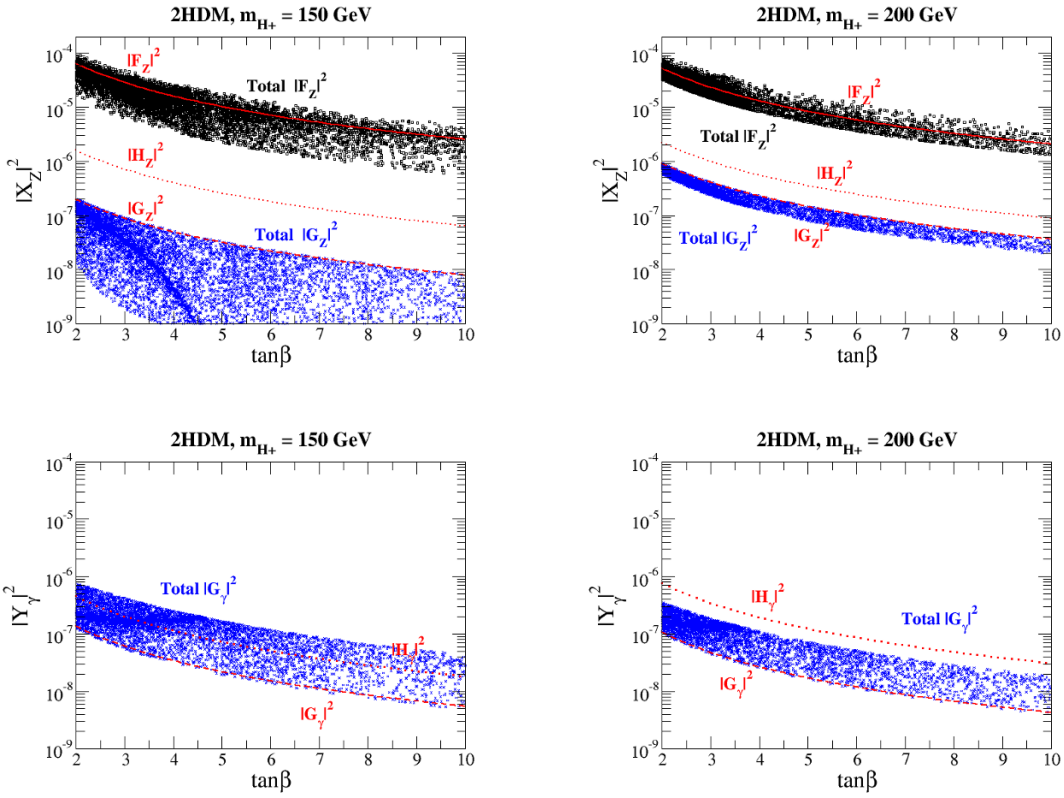

Figure 3. Values of $|X_Z|^2$ ($X = F,\ G$ and H) (upper panels) and $|Y_\gamma|^2$ ($Y = G$ and H) (lower panels) as a function of $\tan\beta$ in the 2HDM with the Type-I or Type-X Yukawa interactions. We take $m_{H^\pm} = 150\,\text{GeV}$ (left panels) and 200 GeV (right panels). In both the panels, $m_H = m_{H^\pm}$ and $\sin(\beta-\alpha) = 1$ are taken. The values of M^2 and m_A^2 are scanned over the ranges of $-400^2 < M^2 < +400^2\,\text{GeV}^2$ and $100 < m_A < 260\ (350)\,\text{GeV}$ in the left (right) panels, respectively. The solid, dashed and dotted (dashed and dotted) curves respectively show the fermion loop contribution to $|F_Z|^2$, $|G_Z|^2$ and $|H_Z|^2$ ($|G_\gamma|^2$ and $|H_\gamma|^2$), while the scatter plots show the total contribution.

contribution to $|F_Z|^2$, $|G_Z|^2$ and $|H_Z|^2$ ($|G_\gamma|^2$ and $|H_\gamma|^2$) whereas the black and blue (blue) scatter plots are the total contribution to $|F_Z|^2$ and $|G_Z|^2$ ($|G_\gamma|^2$), respectively. For the boson loop contribution, we scan the parameters over the intervals $-400^2\,\text{GeV}^2 < M^2 < 400^2\,\text{GeV}^2$ and $100\,\text{GeV} < m_A < 260\ (350)\,\text{GeV}$ in the left (right) panels. We note that $m_A \gtrsim 260\ (350)\,\text{GeV}$ when $m_{H^\pm}(= m_H) = 150\ (200)$ GeV is excluded by the constraint from the S parameter at 95% CL. We also note that only the fermion loop contributes to H_Z and H_γ.

We can see that the value of $|F_Z|^2$ is the biggest of all the form factors as we expected in section 3, because of the m_t^2 dependence. Typically, $|F_Z|^2$ is more than one order of magnitude larger than $|G_Z|^2$ and $|H_Z|^2$. In addition, all the squared form factors decrease as $\tan\beta$ is getting larger, because the top Yukawa coupling is proportional to $\cot\beta$. The maximal allowed value of $|F_Z|^2$ is obtained to be about 10^{-4} at $\tan\beta \simeq 2.5$ in both the cases of $m_{H^\pm} = 150\,\text{GeV}$ and $200\,\text{GeV}$. For the $H^\pm W^\mp\gamma$ vertex, the maximal allowed values of $|G_\gamma|^2$ and $|H_\gamma|^2$ are order of 10^{-6} at $\tan\beta \simeq 2$.

JHEP08(2015)116

Regarding the 3HDM, as we see from eq. (3.21), F_Z is logarithmically enhanced by m_{η_A} in the case of $m_{\eta^\pm} = m_{\eta_H}$. However, a too large mass difference between η_A and $\eta^\pm$ is excluded by the S parameter as shown in figure 1 in the case of $m_{H^\pm} = m_A = m_H$ or $\Delta T = 0$. We thus take a mass difference between $H^\pm$ and A/H with $m_H = m_A$ to avoid the constraint by the effect of non-zero ΔT. From the above reason, we consider the following parameter conditions in the following calculations:

$$\begin{aligned} &m_A = m_H = m_{H^\pm} + 50 \text{ GeV}, && M^2 = m^2_{H^\pm}, \\ &m_{\eta^\pm} = m_{\eta_H} = \frac{1}{2} m_A, \quad m_{\eta_A} > m_{\eta^\pm}, && -10 < \rho_2, \rho_3 < 10. \end{aligned} \tag{5.5}$$

We note that, in this setup, η_H corresponds to the DM candidate. The measured relic abundance of DM[10] can be satisfied by the resonant process of $\eta_H \eta_H \to A/H \to f\bar{f}$.

In figure 4, the values of $|X_Z|^2$ ($X = F$, G and H) and $|Y_\gamma|^2$ ($Y = G$ and H) are respectively shown in the upper and lower panels as a function of $\tan\beta$ with $m_{\eta_A} = 400\,\text{GeV}$. The left (right) panel shows the case of $m_{H^\pm} = 150$ (200) GeV. In the upper panel, the black scatter plots show the values of $|F_Z|^2$. In all the panels, the blue scatter plot and the solid curve respectively represent $|G_V|^2$ and $|H_V|^2$ ($V = Z, \gamma$). Similar to the results in the 2HDM, $|F_Z|^2$ is the biggest of all the squared form factors also in the 3HDM, and all the squared form factors become smaller when $\tan\beta$ becomes large. Remarkably, at $\tan\beta = 2$, we obtain $|F_Z|^2 \simeq 10^{-3}$, which is one order of magnitude larger than $|F_Z|^2$ in the 2HDM.

In figure 5, we show the m_{η_A} dependence of the squared form factors in the case of $\tan\beta = 2.5$. We take $m_{H^\pm} = 150$ (200) GeV in the left (right) panel. The description of the objects in the figure is the same as in figure 4. Clearly, we can see that only $|F_Z|^2$ is enhanced as m_{η_A} is getting larger. The maximal allowed value of $|F_Z|^2$ is about 10^{-3} at $m_{\eta_A} \simeq 500\,\text{GeV}$.

5.2 Branching fractions of $H^\pm$

Next, we discuss the decay branching ratios of $H^\pm$. As we see in figures 4 and 5 that the form factor F_Z is much larger than G_Z and H_Z, we only keep the term proportional to $|F_Z|^2$ for the $H^\pm \to WZ$ decay. When $m_{H^\pm} > m_W + m_Z$, the on-shell decay of $H^\pm \to W^\pm Z$ opens and its decay rate is calculated as

$$\Gamma(H^\pm \to W^\pm Z) = \frac{\sqrt{2} G_F}{16\pi} m^3_{H^\pm} \lambda^{1/2}(x_W, x_Z) c^2_W [\lambda(x_W, x_Z) + 12 x_W x_Z] |F_Z|^2, \tag{5.6}$$

where $x_W = m^2_W/m^2_{H^\pm}$ and $x_Z = m^2_Z/m^2_{H^\pm}$. If $m_{H^\pm}$ is smaller than $m_W + m_Z$, the off-shell decay modes $H^\pm \to W^\pm Z^*$ and $H^\pm \to W^{\pm *} Z$ are allowed. The decay rate with three body

[10] Because the DM phenomenology is not the main topic of this paper, we do not perform the detailed analysis such as the calculation of the (co)annihilation cross sections of the DM candidate.

JHEP08(2015)116

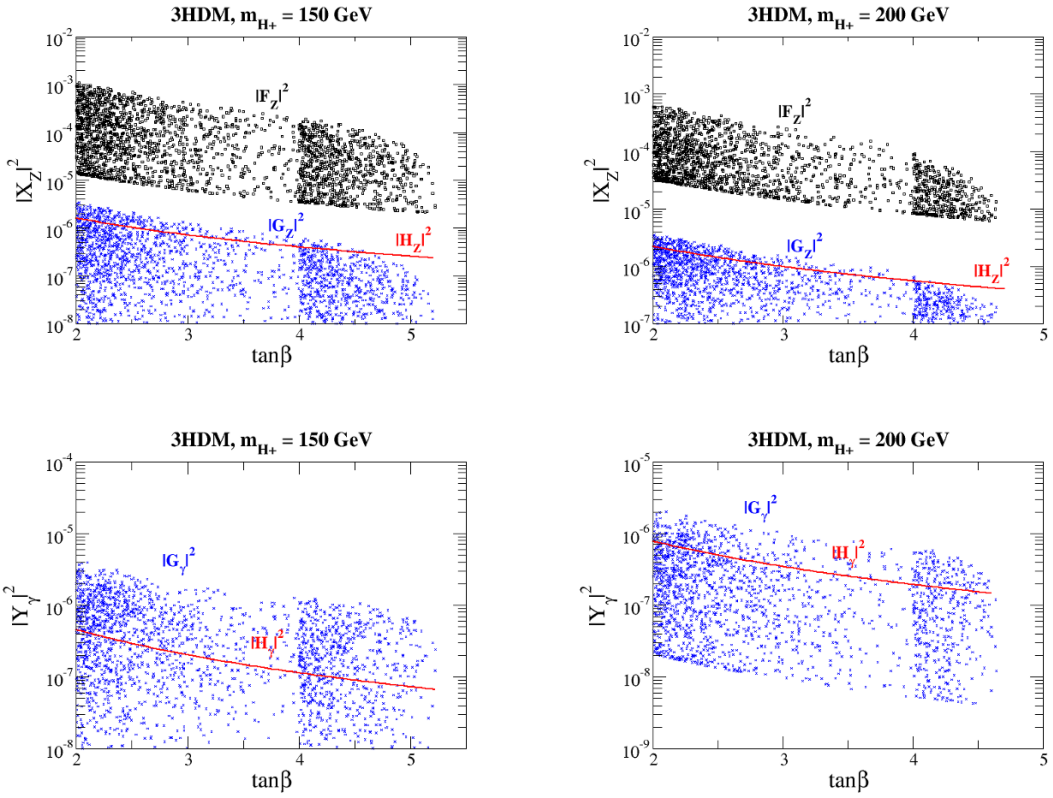

Figure 4. Values of $|X_Z|^2$ ($X = F,\ G$ and H) (upper panels) and $|Y_\gamma|^2$ ($Y = G$ and H) (lower panels) as a function of $\tan\beta$ in the 3HDM with $m_{\eta_A} = 400\,\text{GeV}$. We take $m_{H^\pm} = 150\,\text{GeV}$ (left panels) and 200 GeV (right panels). All the other parameters are taken as given in eq. (5.5). In the upper panel, the black scatter plot shows the values of $|F_Z|^2$. In all the panels, the blue scatter plot and the solid curve respectively represent $|G_V|^2$ and $|H_V|^2$ ($V = Z, \gamma$).

final states is given by

$$\sum_{f,f'}\Gamma(H^\pm\to W^{\pm *}Z\to Zf\bar{f}')=\frac{9g^4m_W^2}{256\pi^3m_{H^\pm}}|F_Z|^2F_3\left(x_Z,x_W\right), \tag{5.7}$$

$$\sum_{f}\Gamma(H^\pm\to W^{\pm}Z^*\to Wf\bar{f})=\frac{3g^4m_Z^2}{512\pi^3m_{H^\pm}}|F_Z|^2\left(7-\frac{40}{3}s_W^2+\frac{160}{9}s_W^4\right)F_3\left(x_W,x_Z\right), \tag{5.8}$$

where

$$F_3(x,y^*)=\frac{\arctan\left[\frac{(1-x)\sqrt{-\lambda(x,y^*)}}{y^*(1+x)-(1-x)^2}\right]+\pi}{4x\sqrt{-\lambda(x,y^*)}}\left[(1-y^*)^3-3x^3+(9y^*+7)x^2-5(1-y^*)^2x\right] \tag{5.9}$$
$$+\frac{1}{24xy^*}\left\{(x-1)[6y^{*2}+y^*(39x-9)+2(1-x)^2]-3y^*[y^{*2}+2y^*(3x-1)-x(3x+4)+1]\ln x\right\}.$$

We note that the argument y^* is for the ratio of squared masses of a virtual gauge boson to that of $H^\pm$, e.g., for the $H^\pm\to W^{\pm *}Z$ case, we should use $F_3(m_Z^2/m_{H^\pm}^2, m_W^2/m_{H^\pm}^2)$.

JHEP08(2015)116

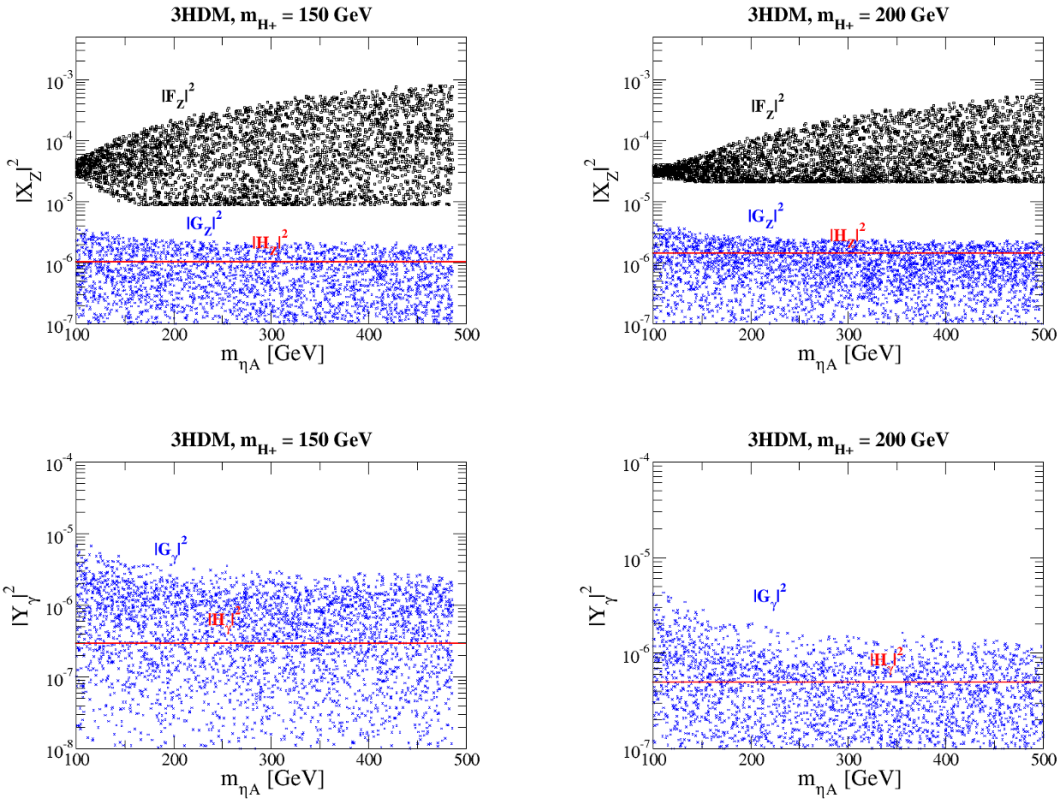

Figure 5. Values of $|X_Z|^2$ ($X = F$, G and H) (upper panels) and $|Y_\gamma|^2$ ($Y = G$ and H) (lower panels) as a function of m_{η_A} in the 3HDM with $\tan\beta = 2.5$. We take $m_{H^\pm} = 150\,\text{GeV}$ (left panels) and 200 GeV (right panels). All the other parameters are taken as given in eq. (5.5). In the upper panel, the black scatter plot shows the values of $|F_Z|^2$. In all the panels, the blue scatter plot and the solid curve respectively represent $|G_V|^2$ and $|H_V|^2$ ($V = Z, \gamma$).

The decay rate for $H^\pm \to W^\pm\gamma$ is given by

$$\Gamma(H^\pm \to W^\pm\gamma) = \frac{\sqrt{2}G_F}{8\pi} m_{H^\pm}^3 (1 - x_W)^3 \left(|G_\gamma|^2 + |H_\gamma|^2\right). \tag{5.10}$$

In figure 6, we show the branching fractions of $H^\pm$ as a function of m_{η_A} in the 3HDM with the Type-I Yukawa interaction. We take $m_{H^\pm} = 150$ (left), 170 (center) and 200 GeV (right). The value of $\tan\beta$ is fixed to be 2.5 in all the panels. In these plots, we scan the values of ρ_2 and ρ_3 in the range of -10 to $+10$ and extract the set of (ρ_2, ρ_3) combinations giving the maximal value of the decay rate $\Gamma(H^\pm \to WZ)$. Further, for the case of $m_{H^\pm} < m_W + m_Z$, we show the branching fraction of $H^\pm \to W^\pm Z$ as the sum of the branching fractions of $H^\pm \to W^\pm Z^*$ and $H^\pm \to W^{\pm *} Z$. In all the plots, the behavior of m_{η_A} in the $H^\pm \to W^\pm Z$ decay is similar to that of $|F_Z|^2$ shown in figure 5. In the case of $m_{H^\pm} = 150\,\text{GeV}$, although $\text{BR}(H^\pm \to W^\pm Z)$ benefits from the enhancement of $|F_Z|^2$, its rate is smaller than $\text{BR}(H^\pm \to W^\pm\gamma)$ when $m_{\eta_A} \lesssim 300\,\text{GeV}$. This can be understood by the suppression of the decay rate of $H^\pm \to W^\pm Z$ due to the off-shell effect of the $W^\pm$ or Z bosons. Therefore, we obtain a larger value of $\text{BR}(H^\pm \to W^\pm Z)$ in the case of

JHEP08(2015)116

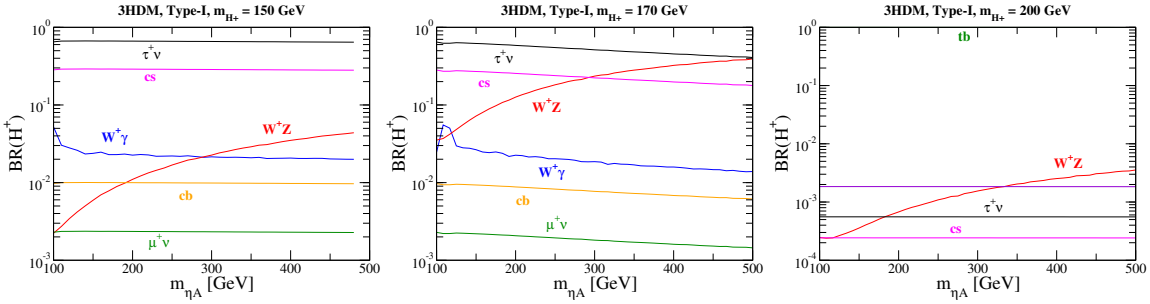

Figure 6. Branching fractions of $H^\pm$ as a function of m_{η_A} in the Type-I Yukawa interaction with $\tan\beta = 2.5$. We take $m_{H^\pm} = 150\,\text{GeV}$ (left), 170 GeV (center) and 200 GeV (right).

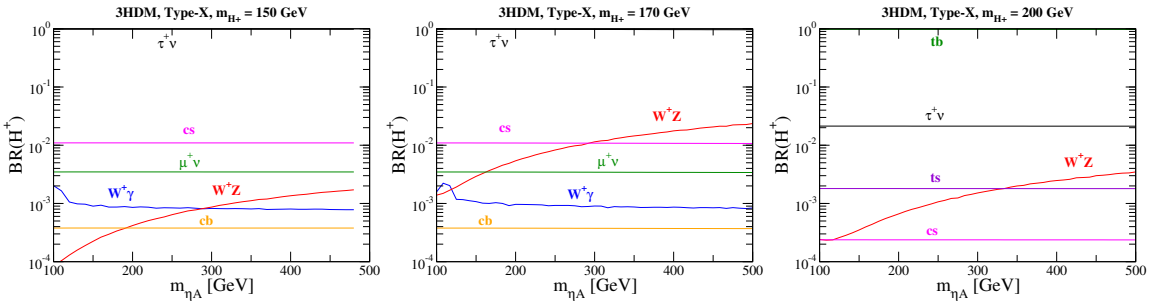

Figure 7. Branching fractions of $H^\pm$ as a function of m_{η_A} in the Type-X Yukawa interaction with $\tan\beta = 2.5$. We take $m_{H^\pm} = 150\,\text{GeV}$ (left), 170 GeV (center) and 200 GeV (right).

$m_{H^\pm} = 170\,\text{GeV}$ because of the smaller off-shell effect. However, once $m_{H^\pm}$ exceeds the top quark mass, both the branching fractions of $H^\pm \to W^\pm Z$ and $H^\pm \to W^\pm\gamma$ are significantly suppressed by the $H^\pm \to tb$ decay. We find that the maximal value of $\text{BR}(H^\pm \to W^\pm Z)$ is about 4%, 40% and 0.4% in the cases of $m_{H^\pm} = 150$, 170 and 200 GeV, respectively.

In figure 7, we also show the branching fraction of $H^\pm$ in the Type-X Yukawa interaction with $\tan\beta = 2.5$. Although we observe a similar behavior of $\text{BR}(H^\pm \to W^\pm Z)$ and $\text{BR}(H^\pm \to W^\pm\gamma)$ as seen in figure 6, their maximal values are smaller than those in the case of the Type-I Yukawa interaction. This is because in the Type-X Yukawa interaction, the decay rate of the $H^\pm \to \tau^\pm\nu$ mode is enhanced by $\tan^2\beta$. Here, the maximal value of $\text{BR}(H^\pm \to W^\pm Z)$ is about 0.2%, 2% and 0.3% in the cases of $m_{H^\pm} = 150$, 170 and 200 GeV, respectively.

5.3 Cross sections at the LHC

Finally, we discuss the signature of the $H^\pm \to W^\pm Z$ and $H^\pm \to W^\pm\gamma$ decays at the LHC. As we showed in section 5.2, when we consider the case of $m_{H^\pm} > m_t + m_b$ both the branching fractions of $H^\pm \to W^\pm Z$ and $H^\pm \to W^\pm\gamma$ are significantly suppressed by the appearance of the $H^\pm \to tb$ decay. In addition, if the $H^\pm$ mass is below the top quark mass, the top decay $t \to H^\pm b$ is the dominant production mode of $H^\pm$ while above it $H^\pm$-strahlung becomes dominant. In reality, the latter is never significant as a means of enabling

JHEP08(2015)116

$H^\pm \to W^\pm Z$ and $H^\pm \to W^\pm \gamma$ detection. We thus focus on the case of $m_{H^\pm} < m_t + m_b$ with the Type-I and Type-X Yukawa interactions in this subsection.

In this case, we expect the signature $pp \to b\bar{b}H^\pm W^\mp \to b\bar{b}W^\pm W^\mp V$ whose cross section $\sigma_S^{\rm top}$ is estimated by

$$\sigma_{S,V}^{\rm top} = 2 \times \sigma_{t\bar{t}} \times [1 - {\rm BR}(t \to H^\pm b)] \times {\rm BR}(t \to H^\pm b) \times {\rm BR}(H^\pm \to W^\pm V), \qquad (5.11)$$

where $\sigma_{t\bar{t}}$ is the top quark pair production cross section at the LHC. In ref. [47], $\sigma_{t\bar{t}} = 923.0$ pb has been obtained with $m_t = 171\,{\rm GeV}$ and $\sqrt{s} = 14\,{\rm TeV}$ at the next-to-next-to leading order using `CTEQ6.6` parton distribution function [48]. As alternative production modes of $H^\pm$ states, especially helpful when the charged Higgs mass is larger than the top quark mass, one should also count the EW productions, e.g., $pp \to H^\pm A$, $pp \to H^\pm H$ and $pp \to H^+H^-$ whose cross sections are determined by the masses of extra Higgs bosons. The cross sections for $H^\pm A$ and $H^\pm H$ productions are the same as long as we take $m_A = m_H$ and $\sin(\beta-\alpha) = 1$. By using these production modes, we can consider $pp \to H^\pm A/H^\pm H \to W^\pm V + X^0$ and $pp \to H^+H^- \to W^\pm V + X^\mp$, where X^0 and $X^\pm$ are respectively the decay product of A/H and $H^\pm$. The signal cross section via the EW production modes are estimated by

$$\sigma_{S,V}^{\rm EW} = (\sigma_{H^\pm A} + \sigma_{H^\pm H} + 2\sigma_{H^+H^-}) \times {\rm BR}(H^\pm \to W^\pm V), \qquad (5.12)$$

where $\sigma_{H^\pm A}$, $\sigma_{H^\pm H}$ and $\sigma_{H^+H^-}$ are respectively the cross sections of $pp \to H^\pm A$, $pp \to H^\pm H$ and $pp \to H^+H^-$. In the cases of $m_{H^\pm} = 130$, 150 and 170 GeV, we obtain $\sigma_{H^\pm A}$ ($\sigma_{H^+H^-}$) = 84 (89), 54 (53) and 36 (34) fb , respectively, at $\sqrt{s} = 14\,{\rm TeV}$ using `CTEQ6L`. For $\sigma_{H^\pm A}$ ($= \sigma_{H^\pm H}$), the above numbers are obtained by summing the H^+A and H^-A processes.

In tables 3 and 4, we show the branching fractions of the $t \to H^\pm b$, $H^\pm \to W^\pm Z$ and $H^\pm \to W^\pm \gamma$ modes and the overall signal cross sections of both the top decay and EW processes estimated by using eqs. (5.11) and (5.12), respectively. The results with the Type-I (X) Yukawa interaction are given in table 3 (4). For the top decay process, the production cross section gets smaller when $m_{H^\pm}$ approaches m_t because of the phase space suppression. Conversely, the branching fraction for $H^\pm \to W^\pm Z$ becomes larger as we already seen in figures 6 and 7. As a result, $\sigma_{S,Z}^{\rm top}$ attains a maximal value around $m_{H^\pm} \simeq 150\,{\rm GeV}$, while $\sigma_{S,\gamma}^{\rm top}$ is simply reduced as $m_{H^\pm}$ becomes larger since ${\rm BR}(H^\pm \to W^\pm\gamma)$ does not encounter any threshold (as $m_{H^\pm} > m_{W^\pm}$). For the EW processes, the reduction of the production cross section ($\sigma_{H^\pm A}$, $\sigma_{H^\pm H}$ and $\sigma_{H^+H^-}$) is milder than that of the top decay process ($\sigma_{t\bar{t}} \times {\rm Br}(t \to H^\pm b)$). Therefore, the signal cross section of the EW processes become larger than the top decay process at $m_{H^\pm} = 170\,{\rm GeV}$. Finally, we note that the signal cross sections in the Type-X case is more than one order of magnitude smaller than those in the Type-I case.

6 Conclusion

We have computed the strength of the $H^\pm W^\mp Z$ and $H^\pm W^\mp \gamma$ vertices at the one-loop level in the 3HDM under a $Z_2 \times \tilde{Z}_2$ symmetry, which defines a Higgs sector with two active doublets and one inert one. We have discussed all the four types of the Yukawa

JHEP08(2015)116

	Type-I	Type-X
$\mathrm{Br}(t \to H^\pm b)$ [%]	(3.3, 1.10, 4.7×10^{-3})	(3.3, 1.1, 4.7×10^{-3})
$\mathrm{Br}(H^\pm \to W^\pm Z)$ [%]	(0.66, 3.5, 33)	(0.025, 0.14, 1.8)
$\mathrm{Br}(H^\pm \to W^\pm \gamma)$ [%]	(1.6, 2.1, 1.6)	(0.059, 0.081, 0.087)
$\sigma^{\mathrm{top}}_{S,Z}$ [fb]	(390, 700, 29)	(15, 28, 1.6)
$\sigma^{\mathrm{top}}_{S,\gamma}$ [fb]	(940, 420, 1.4)	(35, 16, 0.075)
$\sigma^{\mathrm{EW}}_{S,Z}$ [fb]	(2.3, 7.5, 46)	(0.087, 0.30, 2.5)
$\sigma^{\mathrm{EW}}_{S,\gamma}$ [fb]	(5.5, 4.5, 2.2)	(0.20, 0.17, 0.12)

Table 3. The branching fractions and the cross sections in the 3HDM with a Type-I and Type-X Yukawa interaction. We take $\tan\beta = 2.5$ and $m_{\eta_A} = 400\,\mathrm{GeV}$. The numbers in the bracket correspond to the result of $m_{H^\pm}$ =130, 150 and 170 GeV from left to right.

	Type-I	Type-X
$\mathrm{Br}(t \to H^\pm b)$ [%]	(1.3, 0.43, 1.8×10^{-3})	(1.3, 0.43, 1.8×10^{-3})
$\mathrm{Br}(H^\pm \to W^\pm Z)$ [%]	(0.52, 2.7, 26)	(3.0×10^{-3}, 0.016, 0.21)
$\mathrm{Br}(H^\pm \to W^\pm \gamma)$ [%]	(1.1, 1.5, 1.2)	(6.5×10^{-3}, 8.6×10^{-3}, 9.3×10^{-3})
$\sigma^{\mathrm{top}}_{S,Z}$ [fb]	(120, 210, 8.6)	(0.71, 1.3, 0.070)
$\sigma^{\mathrm{top}}_{S,\gamma}$ [fb]	(260, 120, 0.40)	(1.5, 0.68, 3.1×10^{-3})
$\sigma^{\mathrm{EW}}_{S,Z}$ [fb]	(1.8, 5.8, 36)	(0.010, 0.034, 0.29)
$\sigma^{\mathrm{EW}}_{S,\gamma}$ [fb]	(3.8, 3.2, 1.7)	(0.022, 0.018, 0.013)

Table 4. Same as table 3 but for $\tan\beta = 4$.

interactions which are defined by the $\tilde{Z}_2$ charge assignment to the SM fermions. We have taken into account vacuum stability and perturbative unitarity as theoretical constraints, and have considered the bounds from the EW S, T and U parameters, flavour experiments and direct searches for $H^\pm$ states at LEP-II and LHC Run-I. We have seen that the mass of the $H^\pm$ can be smaller than the top quark mass in models with the Type-I and Type-X Yukawa interactions, but not in Type-II and Type-Y. Further, we have shown that, among all the form factors, only F_Z can be enhanced with respect to the 2HDM by taking large mass splittings between η_A and $\eta^\pm$, because of the effect of the inert scalar boson loop contributions.

In particular, we have found that in the 3HDM the squared form factor $|F_Z|^2$ can be one order of magnitude larger than that predicted in the 2HDM under the aforementioned theoretical and experimental constraints. In addition, the branching fraction of the $H^\pm \to W^\pm Z$ mode can be about 4 (0.2)%, 40 (2)% and 0.4 (0.3)% in the cases of $m_{H^\pm} = 150$, 170 and 200 GeV, respectively with the Type-I (Type-X) Yukawa interactions. In contrast, the branching fraction of the $H^\pm \to W^\pm \gamma$ mode is at the few percent level as long as $m_{H^\pm}$ is smaller than the top quark mass in the Type-I and Type-X cases, thus benefiting from

JHEP08(2015)116

very little enhancement with respect to the 2HDM. Such increased rates in the 3HDM stem from loop contributions due to inert Higgs states that are absent in the 2HDM.

Finally, we have discussed signal processes embedding $H^\pm \to W^\pm Z$ and $H^\pm \to W^\pm\gamma$ decays at the LHC. In the light $H^\pm$ scenario, i.e., $m_{H^\pm} < m_t$, with the Type-I and Type-X Yukawa interactions, the top quark decay process $t \to H^\pm b$ is the dominant production mode for $H^\pm$ except for the extreme case of $m_{H^\pm} \lesssim m_t$. In the heavy $H^\pm$ scenario, i.e., $m_{H^\pm} > m_t$, this channel is no longer viable and we have resorted to the $bg \to tH^\pm$ mode. (Herein, we have emulated top production plus decay and $H^\pm$-strahlung via $gg \to tbH^\pm$.) In fact, there are also EW production modes, such as $pp \to H^+H^-$, $pp \to H^\pm A$ and $pp \to H^\pm H$. By combining the production and decay of $H^\pm$'s, we have considered the signal processes $pp \to b\bar{b}W^\pm H^\mp \to b\bar{b}W^+W^-V$, $pp \to H^+H^- \to W^\pm V X^\mp$ and $pp \to H^\pm A/H^\pm H \to W^\pm V X^0$. We have thus computed the ensuing cross sections in all cases and shown that the LHC Run-II has the potential to access $H^\pm \to W^\pm Z$ and/or $H^\pm \to W^\pm\gamma$ decays, certainly for light $H^\pm$'s (at standard luminosity) and possibly for heavy $H^\pm$'s (at very high luminosity). To establish one or the other such signals at the CERN machine may represent circumstantial evidence of a 3HDM sector, as opposed to a 2HDM.

Acknowledgments

S. M. is supported in part through the NExT Institute. D. R. is financed in part by CONACYT-México. K. Y. is fully supported by a JSPS postdoctoral fellowships for research abroad.

A 1PI contributions

Here, we give the analytic expressions for the 1PI diagram contributions to the form factors of the $H^\pm W^\mp V$ ($V = Z,\ \gamma$) vertices and those for the $W^\pm$-$H^\pm$ mixing $\Gamma^{\rm 1PI}_{WH}$. The fermion loop contribution to the $H^\pm W^\mp V$ vertices has been calculated in ref. [11] whereas the boson contribution in the 2HDM has been evaluated in refs. [12, 13]. In addition to these contributions, there are inert scalar boson loop contributions as shown in figure 8.

In the following, we separately show the fermion and boson loop contributions to the form factors denoted by $X^{\rm 1PI}_{V,F}$ and $X^{\rm 1PI}_{V,B}$ ($X = F, G$ and H), respectively. Regarding the boson loop contribution, we only show the contributions from pure scalar loop diagrams, where scalar bosons are running in the triangle and circle type diagrams (see figure 8). There are additional gauge-scalar mixed type diagrams, where one gauge and two active scalar bosons or two gauge and one active scalar bosons run in the triangle part. Because these contributions are proportional to $\cos(\beta-\alpha)$, they vanish or become negligible by taking the SM-like limit $\sin(\beta-\alpha) \to 1$ or taking the SM-like regime $\sin(\beta-\alpha) \simeq 1$, respectively. We thus neglect them here.[11]

In order to express loop functions, we use the Passarino-Veltman functions [49]. Here, we give the integral formulae of some of the functions which we use in the following

[11] The contributions from the gauge-scalar mixed type diagrams are given in ref. [12].

JHEP08(2015)116

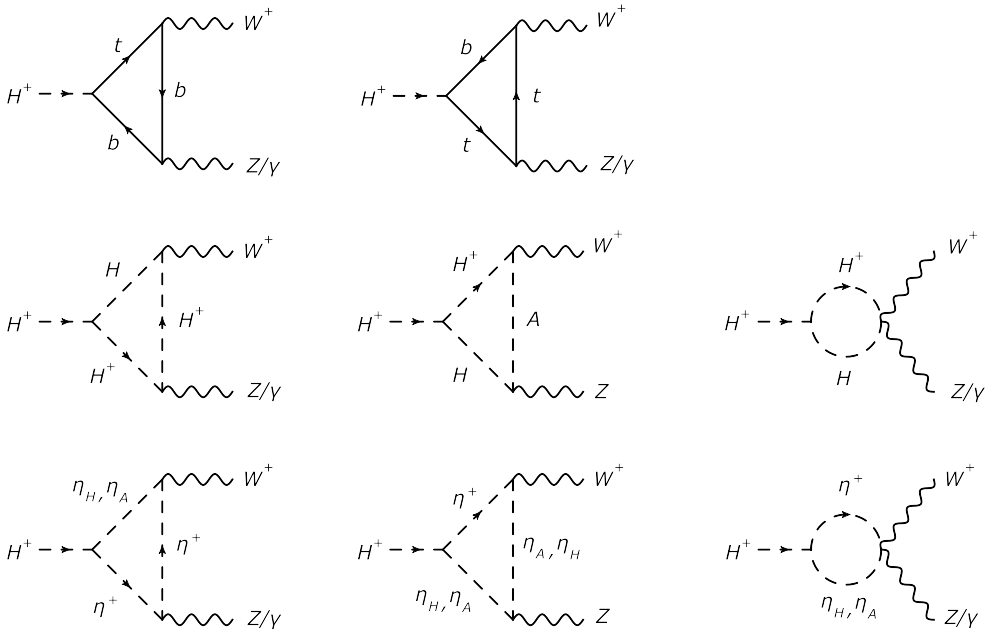

Figure 8. The 1PI diagrams for the $H^{\pm}W^{\mp}Z$ and $H^{\pm}W^{\mp}\gamma$ vertices. The diagrams which vanish in the limit $\sin(\beta-\alpha)=1$ are not displayed.

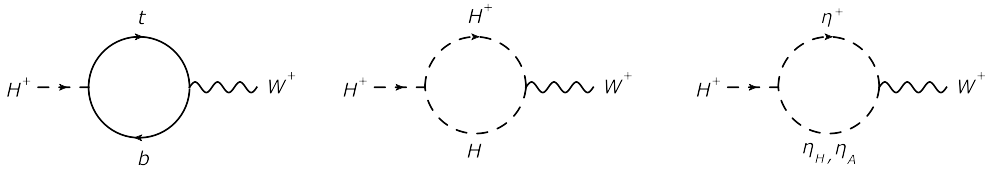

Figure 9. Diagrams giving the $H^{\pm}$-$W^{\mp}$ mixing. The diagrams which vanish in the limit $\sin(\beta-\alpha)=1$ are not displayed.

discussion:

$$B_0(p^2;m_1,m_2) = \Delta - \int_0^1 dx \ln \Delta_B, \tag{A.1a}$$

$$B_1(p^2;m_1,m_2) = -\frac{\Delta}{2} + \int_0^1 dx(1-x)\ln \Delta_B, \tag{A.1b}$$

$$C_0(p_1^2,p_2^2,q^2;m_1,m_2,m_3) = -\int_0^1 dx \int_0^1 dy \frac{y}{\Delta_C}, \tag{A.1c}$$

$$C_{11}(p_1^2,p_2^2,q^2;m_1,m_2,m_3) = -\int_0^1 dx \int_0^1 dy \frac{y(xy-1)}{\Delta_C}, \tag{A.1d}$$

$$C_{12}(p_1^2,p_2^2,q^2;m_1,m_2,m_3) = -\int_0^1 dx \int_0^1 dy \frac{y(y-1)}{\Delta_C}, \tag{A.1e}$$

$$C_{21}(p_1^2,p_2^2,q^2;m_1,m_2,m_3) = -\int_0^1 dx \int_0^1 dy \frac{y(1-xy)^2}{\Delta_C}, \tag{A.1f}$$

$$C_{22}(p_1^2,p_2^2,q^2;m_1,m_2,m_3) = -\int_0^1 dx \int_0^1 dy \frac{y(1-y)^2}{\Delta_C}, \tag{A.1g}$$

JHEP08(2015)116

$$C_{23}(p_1^2,p_2^2,q^2;m_1,m_2,m_3) = -\int_0^1 dx \int_0^1 dy \frac{y(1-xy)(1-y)}{\Delta_C}, \tag{A.1h}$$

$$C_{24}(p_1^2,p_2^2,q^2;m_1,m_2,m_3) = \frac{\Delta}{4} - \frac{1}{2}\int_0^1 dx \int_0^1 dy\, y \ln \Delta_C, \tag{A.1i}$$

where

$$\Delta_B = -x(1-x)p^2 + xm_1^2 + (1-x)m_2^2, \tag{A.2}$$

$$\Delta_C = y^2(p_1 x + p_2)^2 + y[x(p_2^2 - q^2 + m_1^2 - m_2^2) + m_2^2 - m_3^2 - p_2^2] + m_3^2\,. \tag{A.3}$$

In eq. (A.1), Δ is given by

$$\Delta \equiv \frac{1}{\epsilon} - \gamma_E + \ln 4\pi + \ln \mu^2, \tag{A.4}$$

where ϵ appears in the $D(=4-2\epsilon)$ dimensional integral, μ is an arbitrary dimensionful parameter and γ_E is the Euler constant. In the four dimension limit $\epsilon \to 0$, Δ is divergent. We note that this divergent part Δ appears in the following expressions, but it is exactly cancelled in the renormalized variables such as X_Z and X_γ ($X = F,\ G$ and H). We use the shorthand notations like $B_i(p^2;A,B) = B_i(p^2;m_A,m_B)$ and $C_{i,\ ij}(A,B,C) = C_{i,\ ij}(p_1^2,p_2^2,q^2;m_A,m_B,m_C)$.

The fermion loop contribution to $X_Z^{\rm 1PI}$ is given by

$$\begin{aligned}
F_{Z,F}^{\rm 1PI} = {}& \frac{2N_c}{16\pi^2 v^2 c_W}\Big\{ \\
& + m_t^2\xi_t(v_b+a_b)\Big[4C_{24}(t,b,b) - B_0(q^2;m_t,m_b) - B_0(p_W^2;m_b,m_t) - (2m_b^2 - p_Z^2)C_0(t,b,b)\Big] \\
& - m_b^2\xi_b(v_b+a_b)\Big[4C_{24}(t,b,b) - B_0(p_Z^2;m_b,m_b) - B_0(q^2;m_t,m_b) - (m_t^2+m_b^2-p_W^2)C_0(t,b,b)\Big] \\
& - m_b^2\xi_b(v_b-a_b)\Big[B_0(p_Z^2;m_b,m_b) + B_0(p_W^2;m_t,m_b) + (m_t^2+m_b^2-q^2)C_0(t,b,b)\Big] \\
& + 2m_t^2 m_b^2\xi_t(v_b-a_b)C_0(t,b,b)\Big\} + (m_t,\xi_t,v_b,a_b) \leftrightarrow (m_b,-\xi_b,v_t,a_t),
\end{aligned} \tag{A.5}$$

$$\begin{aligned}
G_{Z,F}^{\rm 1PI} = {}& \frac{4N_c m_W^2}{16\pi^2 v^2 c_W}\Big[m_t^2\xi_t(v_b+a_b)(2C_{23}+2C_{12}+C_{11}+C_0) \\
& - m_b^2\xi_b(v_b+a_b)(2C_{23}+C_{12}) - m_b^2\xi_b(v_b-a_b)(C_{12}-C_{11})\Big](t,b,b) \\
& + (m_t,\xi_t,v_b,a_b) \leftrightarrow (m_b,-\xi_b,v_t,a_t),
\end{aligned} \tag{A.6}$$

$$\begin{aligned}
H_{Z,F}^{\rm 1PI} = {}& \frac{4N_c m_W^2}{16\pi^2 v^2 c_W}\Big[m_t^2\xi_t(v_b+a_b)(C_0+C_{11}) - m_b^2\xi_b(v_b+a_b)C_{12} \\
& + m_b^2\xi_b(v_b-a_b)(C_{12}-C_{11})\Big](t,b,b) \\
& + (m_t,\xi_t,v_b,a_b) \leftrightarrow (m_b,+\xi_b,v_t,a_t),
\end{aligned} \tag{A.7}$$

where

$$v_f = \frac{1}{2}T_3^f - s_W^2 Q_f, \quad a_f = \frac{1}{2}T_3^f. \tag{A.8}$$

JHEP08(2015)116

That to $X_\gamma^{\rm 1PI}$ is given by

$$
\begin{aligned}
F_{\gamma,F}^{\rm 1PI} = \frac{2N_cQ_b}{16\pi^2v^2c_{_W}}\Big\{ & \\
& + m_t^2\xi_t\Big[4C_{24}(t,b,b) - B_0(q^2;m_t,m_b) - B_0(p_{_W}^2;m_b,m_t) - (2m_b^2-p_\gamma^2)C_0(t,b,b)\Big] \\
& - m_b^2\xi_b\Big[4C_{24}(t,b,b) - B_0(p_{_Z}^2;m_b,m_b) - B_0(q^2;m_t,m_b) - (m_t^2+m_b^2-p_{_W}^2)C_0(t,b,b)\Big] \\
& - m_b^2\xi_b\Big[B_0(p_{_Z}^2;m_b,m_b) + B_0(p_{_W}^2;m_t,m_b) + (m_t^2+m_b^2-q^2)C_0(t,b,b)\Big] \\
& + 2m_t^2m_b^2\xi_tC_0(t,b,b)\Big\} + (m_t,\xi_t,Q_b) \leftrightarrow (m_b,\text{–}\xi_b,Q_t), \qquad \text{(A.9)} \\
G_{\gamma,F}^{\rm 1PI} = \frac{4N_cQ_bm_{_W}^2}{16\pi^2v^2c_{_W}}\Big[& m_t^2\xi_t(2C_{23}+2C_{12}+C_{11}+C_0) \qquad \text{(A.10)} \\
& - m_b^2\xi_b(2C_{23}+C_{12}) - m_b^2\xi_b(C_{12}-C_{11})\Big](t,b,b) + (m_t,\xi_t,Q_b) \leftrightarrow (m_b,\text{–}\xi_b,Q_t), \\
H_{Z,F}^{\rm 1PI} = \frac{4N_cQ_bm_{_W}^2}{16\pi^2v^2c_{_W}}\Big[& m_t^2\xi_t(C_0+C_{11}) - m_b^2\xi_bC_{12} + m_b^2\xi_b(C_{12}-C_{11})\Big](t,b,b) \\
& + (m_t,\xi_t,Q_b) \leftrightarrow (m_b,\text{+}\xi_b,Q_t). \qquad \text{(A.11)}
\end{aligned}
$$

The boson loop contribution is given by

$$
\begin{aligned}
F_{Z,B}^{\rm 1PI} = \frac{1}{16\pi^2vc_{_W}}\Big\{ & \qquad \text{(A.12)} \\
& + \lambda_{H^+H^-H}\sin(\beta-\alpha)\Big[(2-4s_{_W}^2)C_{24}(H,H^\pm,H^\pm) \\
& - 2C_{24}(H^\pm,A,H) + s_{_W}^2B_0(q^2;H^\pm,H)\Big] \\
& - \lambda_{H^+\eta^-\eta_H}\Big[(2-4s_{_W}^2)C_{24}(\eta_H,\eta^\pm,\eta^\pm) - 2C_{24}(\eta^\pm,\eta_A,\eta_H) + s_{_W}^2B_0(q^2;\eta^\pm,\eta_H)\Big] \\
& - \lambda_{H^+\eta^-\eta_A}\Big[(2-4s_{_W}^2)C_{24}(\eta_A,\eta^\pm,\eta^\pm) - 2C_{24}(\eta^\pm,\eta_H,\eta_A) + s_{_W}^2B_0(q^2;\eta^\pm,\eta_A)\Big]\Big\}, \\
G_{Z,B}^{\rm 1PI} = \frac{m_{_W}^2}{16\pi^2vc_{_W}}\Big\{ & \\
& + \lambda_{H^+H^-H}\sin(\beta-\alpha)\Big[(2-4s_{_W}^2)(C_{12}+C_{23})(H,H^\pm,H^\pm) - 2(C_{12}+C_{23})(H^\pm,A,H)\Big] \\
& - \lambda_{H^+\eta^-\eta_H}\Big[(2-4s_{_W}^2)(C_{12}+C_{23})(\eta_H,\eta^\pm,\eta^\pm) - 2(C_{12}+C_{23})(\eta^\pm,\eta_A,\eta_H)\Big] \\
& - \lambda_{H^+\eta^-\eta_A}\Big[(2-4s_{_W}^2)(C_{12}+C_{23})(\eta_A,\eta^\pm,\eta^\pm) - 2(C_{12}+C_{23})(\eta^\pm,\eta_H,\eta_A)\Big]\Big\}, \qquad \text{(A.13)} \\
F_{\gamma,B}^{\rm 1PI} = \frac{s_{_W}}{16\pi^2v}\Big\{ & \lambda_{H^+H^-H}\sin(\beta-\alpha)[4C_{24}(H,H^\pm,H^\pm) - B_0(q^2;H^\pm,H)] \\
& - \lambda_{H^+\eta^-\eta_H}[4C_{24}(\eta_H,\eta^\pm,\eta^\pm) - B_0(q^2;\eta^\pm,\eta_H)] \\
& - \lambda_{H^+\eta^-\eta_A}[4C_{24}(\eta_A,\eta^\pm,\eta^\pm) - B_0(q^2;\eta^\pm,\eta_A)]\Big\}, \qquad \text{(A.14)} \\
G_{\gamma,B}^{\rm 1PI} = \frac{4m_{_W}^2s_{_W}}{16\pi^2v}\Big[& \lambda_{H^+H^-H}\sin(\beta-\alpha)(C_{12}+C_{23})(H,H^\pm,H^\pm) \\
& - \lambda_{H^+\eta^-\eta_H}(C_{12}+C_{23})(\eta_H,\eta^\pm,\eta^\pm) - \lambda_{H^+\eta^-\eta_A}(C_{12}+C_{23})(\eta_A,\eta^\pm,\eta^\pm)\Big], \qquad \text{(A.15)}
\end{aligned}
$$

JHEP08(2015)116

and

$$H^{1\mathrm{PI}}_{Z,B} = H^{1\mathrm{PI}}_{\gamma,B} = 0, \tag{A.16}$$

where

$$\lambda_{H^+H^-H} = \frac{1}{v}\Big[(m_H^2 - M^2)(\cot\beta - \tan\beta)\sin(\beta-\alpha) - (2m_{H^\pm}^2 + m_H^2 - 2M^2)\cos(\beta-\alpha)\Big], \tag{A.17}$$

$$\lambda_{H^\pm\eta^\mp\eta_H} = \frac{v}{4}(\rho_2 + \rho_3 - \sigma_2 - \sigma_3)\sin 2\beta, \tag{A.18}$$

$$\lambda_{H^\pm\eta^\mp\eta_A} = \pm\frac{v}{4}(\rho_2 - \rho_3 - \sigma_2 + \sigma_3)\sin 2\beta. \tag{A.19}$$

We note that the above expressions are obtained by extracting the coefficient of the scalar trilinear vertex, i.e., $\mathcal{L} = +\lambda_{\phi_1\phi_2\phi_3}\phi_1\phi_2\phi_3 + \cdots$.

The fermion and boson loop contributions to the $W^\pm$-$H^\pm$ mixing, i.e., $\Gamma^{1\mathrm{PI}}_{WH}(p^2)_F$ and $\Gamma^{1\mathrm{PI}}_{WH}(p^2)_B$, respectively, are given by:

$$\Gamma^{1\mathrm{PI}}_{WH}(p^2)_F = \frac{i}{16\pi^2}\frac{4m_W}{v^2}N_c[m_t^2\xi_t(B_0+B_1) - m_b^2\xi_b B_1](p^2; m_t, m_b), \tag{A.20}$$

$$\begin{aligned}\Gamma^{1\mathrm{PI}}_{WH}(p^2)_B = \frac{i}{16\pi^2}\frac{m_W}{v}\Big[&\lambda_{H^+H^-H}\sin(\beta-\alpha)(2B_1+B_0)(p^2; m_{H^\pm}, m_H) \\ &+ \lambda_{\eta^+\eta^-\eta_H}(2B_1+B_0)(p^2; m_{\eta^\pm}, m_{\eta_H}) + i\lambda_{\eta^+\eta^-\eta_A}(2B_1+B_0)(p^2; m_{\eta^\pm}, m_{\eta_A})\Big].\end{aligned} \tag{A.21}$$

The counter term contribution is then obtained from the above $W^\pm$-$H^\pm$ mixing via eq. (3.19):

$$\delta F_{Z,F} = \frac{4s_W^2 N_c}{16\pi^2 v^2 c_W}[m_t^2\xi_t(B_0+B_1) - m_b^2\xi_b B_1](q^2; t, b), \tag{A.22}$$

$$\begin{aligned}\delta F_{Z,B} = \frac{s_W^2}{16\pi^2 v c_W}\Big[&\lambda_{H^+H^-H}\sin(\beta-\alpha)(2B_1+B_0)(q^2; H^\pm, H) \\ &- \lambda_{H^+\eta^-\eta_H}(2B_1+B_0)(q^2; \eta^\pm, \eta_H) - \lambda_{H^+\eta^-\eta_A}(2B_1+B_0)(q^2; \eta^\pm, \eta_A)\Big],\end{aligned} \tag{A.23}$$

$$\delta F_{\gamma,F/B} = -\frac{c_W}{s_W}\delta F_{Z,F/B}. \tag{A.24}$$

Using the above analytic expressions, we can directly check the relation from the Ward identity in eq. (3.16), i.e., $(F^{1\mathrm{PI}}_\gamma + \delta F_\gamma) = G^{1\mathrm{PI}}_\gamma(1 - m_W^2/m_{H^\pm}^2)/2$.

References

[1] ATLAS collaboration, *Measurements of Higgs boson production and couplings in diboson final states with the ATLAS detector at the LHC*, *Phys. Lett.* **B 726** (2013) 88 [*Erratum ibid.* **B 734** (2014) 406] [arXiv:1307.1427] [INSPIRE].

JHEP08(2015)116

[2] ATLAS collaboration, *Measurements of Higgs boson production and couplings in the four-lepton channel in pp collisions at center-of-mass energies of 7 and 8 TeV with the ATLAS detector*, *Phys. Rev.* **D 91** (2015) 012006 [arXiv:1408.5191] [INSPIRE].

[3] CMS collaboration, *Measurement of Higgs boson production and properties in the WW decay channel with leptonic final states*, *JHEP* **01** (2014) 096 [arXiv:1312.1129] [INSPIRE].

[4] CMS collaboration, *Precise determination of the mass of the Higgs boson and tests of compatibility of its couplings with the standard model predictions using proton collisions at 7 and 8 TeV*, *Eur. Phys. J.* **C 75** (2015) 212 [arXiv:1412.8662] [INSPIRE].

[5] J.F. Gunion, H.E. Haber, G.L. Kane and S. Dawson, *The Higgs Hunter's Guide*, *Front. Phys.* **80** (2000) 1 [INSPIRE].

[6] A. Zee, *A Theory of Lepton Number Violation, Neutrino Majorana Mass and Oscillation*, *Phys. Lett.* **B 93** (1980) 389 [*Erratum ibid.* **B 95** (1980) 461] [INSPIRE].

[7] R. Barbieri, L.J. Hall and V.S. Rychkov, *Improved naturalness with a heavy Higgs: An Alternative road to LHC physics*, *Phys. Rev.* **D 74** (2006) 015007 [hep-ph/0603188] [INSPIRE].

[8] T.D. Lee, *A Theory of Spontaneous T Violation*, *Phys. Rev.* **D 8** (1973) 1226 [INSPIRE].

[9] S. Weinberg, *Gauge Theory of CP-violation*, *Phys. Rev. Lett.* **37** (1976) 657 [INSPIRE].

[10] J.A. Grifols and A. Mendez, *The $WZH^{\pm}$ Coupling in* SU(2) × U(1) *Gauge Models*, *Phys. Rev.* **D 22** (1980) 1725 [INSPIRE].

[11] M. Capdequi Peyranere, H.E. Haber and P. Irulegui, *$H^{\pm} \to W^{\pm}\gamma$ and $H^{\pm} \to W^{\pm}Z$ in two Higgs doublet models. 1. The large fermion mass limit*, *Phys. Rev.* **D 44** (1991) 191 [INSPIRE].

[12] S. Kanemura, *Enhancement of loop induced $H^{\pm}W^{\mp}Z^0$ vertex in two Higgs doublet model*, *Phys. Rev.* **D 61** (2000) 095001 [hep-ph/9710237] [INSPIRE].

[13] S. Kanemura, *Possible enhancement of the $e^+e^- \to H^{\pm}W^{\mp}$ cross-section in the two Higgs doublet model*, *Eur. Phys. J.* **C 17** (2000) 473 [hep-ph/9911541] [INSPIRE].

[14] E. Asakawa and S. Kanemura, *The $H^{\pm}W^{\mp}Z0$ vertex and single charged Higgs boson production via W Z fusion at the large hadron collider*, *Phys. Lett.* **B 626** (2005) 111 [hep-ph/0506310] [INSPIRE].

[15] E. Asakawa, S. Kanemura and J. Kanzaki, *Potential for measuring the $H^{\pm}W^{\mp}Z0$ vertex from WZ fusion at the Large Hadron Collider*, *Phys. Rev.* **D 75** (2007) 075022 [hep-ph/0612271] [INSPIRE].

[16] S. Godfrey and K. Moats, *Exploring Higgs Triplet Models via Vector Boson Scattering at the LHC*, *Phys. Rev.* **D 81** (2010) 075026 [arXiv:1003.3033] [INSPIRE].

[17] S. Kanemura, K. Yagyu and K. Yanase, *Testing Higgs models via the $H^{\pm}W^{\mp}Z$ vertex by a recoil method at the International Linear Collider*, *Phys. Rev.* **D 83** (2011) 075018 [arXiv:1103.0493] [INSPIRE].

[18] B. Grzadkowski, O.M. Ogreid, P. Osland, A. Pukhov and M. Purmohammadi, *Exploring the CP-Violating Inert-Doublet Model*, *JHEP* **06** (2011) 003 [arXiv:1012.4680] [INSPIRE].

[19] B. Grzadkowski, O.M. Ogreid and P. Osland, *Natural Multi-Higgs Model with Dark Matter and CP-violation*, *Phys. Rev.* **D 80** (2009) 055013 [arXiv:0904.2173] [INSPIRE].

JHEP08(2015)116

[20] V. Keus, S.F. King and S. Moretti, *Phenomenology of the inert (2+1) and (4+2) Higgs doublet models*, *Phys. Rev.* **D 90** (2014) 075015 [arXiv:1408.0796] [INSPIRE].

[21] V. Keus, S.F. King, S. Moretti and D. Sokolowska, *Dark Matter with Two Inert Doublets plus One Higgs Doublet*, *JHEP* **11** (2014) 016 [arXiv:1407.7859] [INSPIRE].

[22] S.L. Glashow and S. Weinberg, *Natural Conservation Laws for Neutral Currents*, *Phys. Rev.* **D 15** (1977) 1958 [INSPIRE].

[23] V.D. Barger, J.L. Hewett and R.J.N. Phillips, *New Constraints on the Charged Higgs Sector in Two Higgs Doublet Models*, *Phys. Rev.* **D 41** (1990) 3421 [INSPIRE].

[24] Y. Grossman, *Phenomenology of models with more than two Higgs doublets*, *Nucl. Phys.* **B 426** (1994) 355 [hep-ph/9401311] [INSPIRE].

[25] A.G. Akeroyd, *Nonminimal neutral Higgs bosons at LEP-2*, *Phys. Lett.* **B 377** (1996) 95 [hep-ph/9603445] [INSPIRE].

[26] M. Aoki, S. Kanemura, K. Tsumura and K. Yagyu, *Models of Yukawa interaction in the two Higgs doublet model and their collider phenomenology*, *Phys. Rev.* **D 80** (2009) 015017 [arXiv:0902.4665] [INSPIRE].

[27] J.F. Gunion and H.E. Haber, *The CP conserving two Higgs doublet model: The approach to the decoupling limit*, *Phys. Rev.* **D 67** (2003) 075019 [hep-ph/0207010] [INSPIRE].

[28] P.S.B. Dev and A. Pilaftsis, *Maximally Symmetric Two Higgs Doublet Model with Natural Standard Model Alignment*, *JHEP* **12** (2014) 024 [arXiv:1408.3405] [INSPIRE].

[29] T. Abe and R. Kitano, *Phenomenology of Partially Composite Standard Model*, *Phys. Rev.* **D 88** (2013) 015019 [arXiv:1305.2047] [INSPIRE].

[30] A. Pomarol and R. Vega, *Constraints on CP-violation in the Higgs sector from the rho parameter*, *Nucl. Phys.* **B 413** (1994) 3 [hep-ph/9305272] [INSPIRE].

[31] S. Kanemura, Y. Okada, E. Senaha and C.P. Yuan, *Higgs coupling constants as a probe of new physics*, *Phys. Rev.* **D 70** (2004) 115002 [hep-ph/0408364] [INSPIRE].

[32] S. Kanemura, M. Kikuchi and K. Yagyu, *Fingerprinting the extended Higgs sector using one-loop corrected Higgs boson couplings and future precision measurements*, *Nucl. Phys.* **B 896** (2015) 80 [arXiv:1502.07716] [INSPIRE].

[33] S. Moretti and K. Yagyu, *Constraints on Parameter Space from Perturbative Unitarity in Models with Three Scalar Doublets*, *Phys. Rev.* **D 91** (2015) 055022 [arXiv:1501.06544] [INSPIRE].

[34] M.E. Peskin and T. Takeuchi, *A new constraint on a strongly interacting Higgs sector*, *Phys. Rev. Lett.* **65** (1990) 964 [INSPIRE].

[35] M. Baak et al., *The Electroweak Fit of the Standard Model after the Discovery of a New Boson at the LHC*, *Eur. Phys. J.* **C 72** (2012) 2205 [arXiv:1209.2716] [INSPIRE].

[36] M. Misiak et al., *Updated NNLO QCD predictions for the weak radiative B-meson decays*, *Phys. Rev. Lett.* **114** (2015) 221801 [arXiv:1503.01789] [INSPIRE].

[37] O. Eberhardt, U. Nierste and M. Wiebusch, *Status of the two-Higgs-doublet model of type-II*, *JHEP* **07** (2013) 118 [arXiv:1305.1649] [INSPIRE].

[38] T. Hermann, M. Misiak and M. Steinhauser, $\bar{B} \to X_s\gamma$ *in the Two Higgs Doublet Model up to Next-to-Next-to-Leading Order in QCD*, *JHEP* **11** (2012) 036 [arXiv:1208.2788] [INSPIRE].

JHEP08(2015)116

[39] F. Mahmoudi and O. Stal, *Flavor constraints on the two-Higgs-doublet model with general Yukawa couplings*, *Phys. Rev.* **D 81** (2010) 035016 [arXiv:0907.1791] [INSPIRE].

[40] LEP, DELPHI, OPAL, ALEPH and L3 collaborations, G. Abbiendi et al., *Search for Charged Higgs bosons: Combined Results Using LEP Data*, *Eur. Phys. J.* **C 73** (2013) 2463 [arXiv:1301.6065] [INSPIRE].

[41] ATLAS collaboration, *Search for charged Higgs bosons decaying via $H^{\pm} \to \tau^{\pm}\nu$ in fully hadronic final states using pp collision data at $\sqrt{s} = 8$ TeV with the ATLAS detector*, *JHEP* **03** (2015) 088 [arXiv:1412.6663] [INSPIRE].

[42] M. Guchait and S. Moretti, *Improving the discovery potential of charged Higgs bosons at Tevatron run II*, *JHEP* **01** (2002) 001 [hep-ph/0110020] [INSPIRE].

[43] A.G. Akeroyd, S. Moretti and J. Hernandez-Sanchez, *Light charged Higgs bosons decaying to charm and bottom quarks in models with two or more Higgs doublets*, *Phys. Rev.* **D 85** (2012) 115002 [arXiv:1203.5769] [INSPIRE].

[44] S. Moretti, A. Akeroyd and J. Hernández-Sánchez, *$H^{\pm} \to cb$ in models with two or more Higgs doublets*, PoS(Charged2014)025 [arXiv:1409.7596] [INSPIRE].

[45] PARTICLE DATA GROUP collaboration, K.A. Olive et al. *Review of Particle Physics*, *Chin. Phys.* **C 38** (2014) 090001 [INSPIRE].

[46] H. Fusaoka and Y. Koide, *Updated estimate of running quark masses*, *Phys. Rev.* **D 57** (1998) 3986 [hep-ph/9712201] [INSPIRE].

[47] U. Langenfeld, S. Moch and P. Uwer, *Measuring the running top-quark mass*, *Phys. Rev.* **D 80** (2009) 054009 [arXiv:0906.5273] [INSPIRE].

[48] P.M. Nadolsky et al., *Implications of CTEQ global analysis for collider observables*, *Phys. Rev.* **D 78** (2008) 013004 [arXiv:0802.0007] [INSPIRE].

[49] G. Passarino and M.J.G. Veltman, *One Loop Corrections for e^+e^- Annihilation Into $\mu^+\mu^-$ in the Weinberg Model*, *Nucl. Phys.* **B 160** (1979) 151 [INSPIRE].

JHEP08(2015)116